2011

A Computational Simulation of Supercritical Carbon Dioxide and Ethanol Capillary Flow

Thomas W. Furlong
University of Massachusetts Amherst, thomas.furlong.14@gmail.com

Follow this and additional works at: http://scholarworks.umass.edu/theses

Part of the Mechanical Engineering Commons

A COMPUTATIONAL SIMULATION OF SUPERCRITICAL CARBON DIOXIDE AND ETHANOL CAPILLARY FLOW

A Thesis Presented

by

THOMAS FURLONG

Submitted to the Graduate School of the
University of Massachusetts Amherst in partial fulfillment
of the requirements for the degree of

MASTERS OF SCIENCE IN MECHANICAL ENGINEERING

September 2011

Mechanical and Industrial Engineering

A COMPUTATIONAL SIMULATION OF SUPERCRITICAL CARBON DIOXIDE AND ETHANOL CAPILLARY FLOW

A Thesis Presented

by

THOMAS FURLONG

Approved as to style and content by:

_____
David P. Schmidt, Chair

_____
James J. Watkins, Member

_____
Stephen de Bruyn Kops, Member

                              _____
                              Donald Fisher, Department Chair
                              Mechanical and Industrial Engineering

ABSTRACT

A COMPUTATIONAL SIMULATION OF SUPERCRITICAL CARBON DIOXIDE AND ETHANOL CAPILLARY FLOW

SEPTEMBER 2011

THOMAS FURLONG

B.S., UNIVERSITY OF NOTRE DAME DU LAC

M.S.M.E., UNIVERSITY OF MASSACHUSETTS AMHERST

Directed by: Professor David P. Schmidt

Homogenous and separated flow methods have been presented for use in the capillary tube section of the Plasma Rapid Expansion of Supercritical Solutions (PRESS) process using a carbon dioxide and ethanol mixture as the working fluid. Each method was validated against experimental expansion processes using pure carbon dioxide, isobutane, and R-134a. The results have indicated that both the homogenous flow method and the separated flow method produce results within an acceptable margin of error. By accounting for the phase interactions the separated flow method produces more accurate results with mean errors of 8.03%, 4.57%, and 5.77% for carbon dioxide, isobutane, and R-134a, respectively. In comparison, the mean errors of the homogenous method were 8.17%, 5.4%, and 8.55%, respectively. The homogenous and separated flow methods were shown to be statistically and significantly different for 95% confidence, which demonstrates that the accuracy of capillary flow simulation can be increased through the use of the separated flow method. A method to extend

the methods for the mixture of carbon dioxide and ethanol was implemented in a limited fashion. Under certain conditions the carbon dioxide and ethanol mixture results in the trivial root problem associated with the cubic compressibility equation. As literature on the subject of the trivial root problem is limited, the expansion process was focused on a region where three real roots exist to the compressibility equation. A simulation of a carbon dioxide and ethanol mixture expansion process was successfully implemented at a low temperature using the homogenous flow method. For validation, a VLE diagram was created for the mixture and compared adequately with experimental results.

TABLE OF CONTENTS

LIST OF TABLES

LIST OF FIGURES

CHAPTER 1

INTRODUCTION

Supercritical fluids have become increasingly prevalent over the past 30 years, due in part to processes such as Supercritical Fluid Extraction (SFE) and the Rapid Expansion of Supercritical Solutions (RESS). This increase in industrial use caused an increase in research leading to a method that utilizes components of both SFE and RESS. This new process, termed the Plasma Rapid Expansion of Supercritical Solutions (PRESS), is an expansion process, shown in Figure 1.1, in which a supercritical fluid travels through an expansion device centered around a capillary tube, (III), and exits into an expansion chamber, (IV and V). Placed within the expansion chamber is a plasma stream, (e), which is angled perpendicular to the direction of the flow.

The process is intended to utilize an increase of solvating power associated with a fluid when it is compressed above the critical point and into the supercritical region [55]. Within the supercritical region, small pressure changes can cause large density changes, varying from liquid to gas like densities, that lead to the increase in solvating power [44]. The increased solvating power of the supercritical fluid allows it to be utilized as a solvent in order to dissolve a precursor into the flow. The precursor could be a solid or liquid that one might want in the form of a powder or fine particle, such as TiO_2, napthalene, benzoic acid, griscofulvin, and β-sitosterol [37]. The mixture is expanded across the device, causing the solvating power of the supercritical fluid to decrease and therefore the precursor to precipitate into fine particles. The precipitation is due to nucleation and growth, which is driven by the supersaturation (S) of the working fluid, given by Equation (1.1) [36].
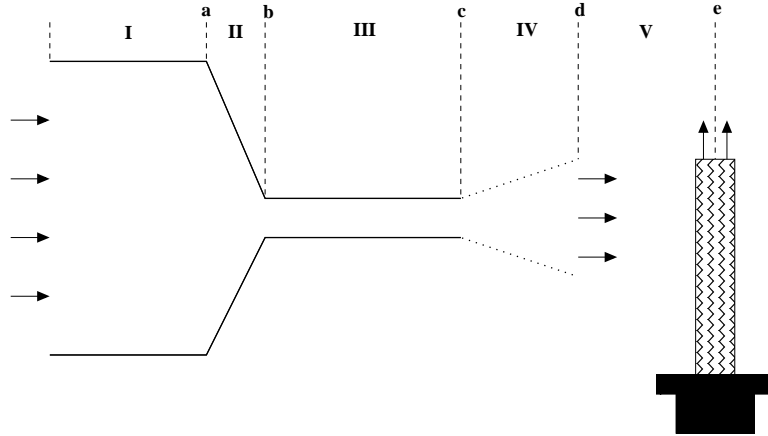
Figure 1.1: Flow Regions within a typical PRESS process.
(**I**) Pre-expansion/Extraction Conditions; (**II**) Capillary Inlet; (**III**) Capillary Tube;
(**IV**) Supersonic Free Jet; (**V**) Subsonic Free Jet. Adapted from Helfgen et al. [37]

$$S = \frac{\phi_{ext} y^*_{ext}}{\phi y^*} \tag{1.1}$$

The fugacity coefficient, ϕ, and equilibrium mole fraction, y^*, are found for the instantaneous pressure and temperature, while ϕ_{ext} and y^*_{ext} are defined for the extraction conditions (point a in Figure 1.1). The fugacity coefficient, given in Equation (1.2), accounts for the non-ideality of the supercritical fluid [36].

$$\phi = \frac{f}{P} \tag{1.2}$$

The precipitation will continue to occur until the plasma stream is reached at which point the particles will be carried by the stream to a substrate. As the process continues, the particles on the substrate will form a thin film that, depending on the material of the precursor, could be used for several applications, from solar panels to pharmaceuticals.

The supercritical fluid typically utilized for the PRESS process consists of a mixture of carbon dioxide (CO_2) and ethanol. The CO_2 is a useful cosolvent due to its low critical pressure, 7.38 MPa, while ethanol is added to increase the solvating

power of the mixture. An ethanol/CO_2 mixture, as opposed to pure CO_2, has been shown to dramatically increase, by a factor of 25, the solubility of a precursor in the supercritical fluid [72]. This is due to the fact that the low solubility of polar precursors in non-polar solvents, such as CO_2, can be increased with the addition of a polar cosolvent, such as ethanol [21].

1.1 Rapid Expansion of Supercritical Solutions
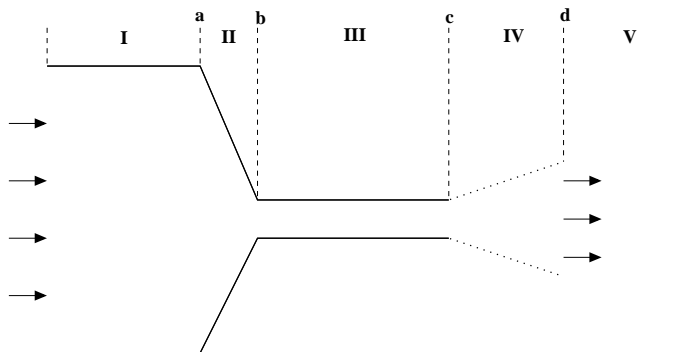
Figure 1.2: Flow Regions within a typical RESS process.
(**I**) Pre-expansion/Extraction Conditions; (**II**) Capillary Inlet; (**III**) Capillary Tube; (**IV**) Supersonic Free Jet; (**V**) Subsonic Free Jet. Adapted from Helfgen et al. [37]

The expansion process of PRESS is based upon the established RESS process shown in Figure 1.2. The expansion device for RESS is identical to the one for PRESS, shown in Figure 1.1, except there is no plasma stream at the end of the expansion chamber, denoted by regions IV and V. While this difference may seem trivial to the internal flow of the device, the typical RESS process only uses a single supercritical fluid as a solvent. Due to the similarities of the process and lack of literature focused on the PRESS process, the RESS process will be utilized for benchmarking and investigative purposes.

The flow of the RESS process can be divided into five sections. Sections I and II are the pre-expansion conditions and the capillary inlet, respectively, that provide the fluid at its initial conditions and directs the flow into the capillary tube, section III.

3

The capillary tube flow has the most complicated flow within the expansion device and therefore is the focus of the research. At the outlet exists the expansion chamber of the device, which contains a supersonic and a subsonic region of flow denoted by sections IV and V, respectively.

1.1.1 Capillary Flow

Capillary tubes, such as those utilized within the RESS and PRESS processes, have been extensively researched over the years due to their multiple uses for fluid expansion and refrigerant control within small and household refrigerator systems, freezers, dehumidifiers, and air conditioners [26, 47, 50]. While a capillary tube, shown in Figure 1.3, can have varying lengths and diameters, it is generally understood to be a long thin tube with a length to diameter ratio greater than 100 and a diameter less than 1 mm. The basic flow properties of an expansion process utilizing a capillary tube will be the same no matter the application. Though the flow can become more complex through the addition of solid particle growth, as in the case of RESS and PRESS processes.

In the case of an adiabatic capillary, the expansion through the tube simplifies to a basic Fanno flow. Fanno flow is governed by viscous choking in which frictional effects drive the flow towards the point of maximum entropy for the local stagnation pressure
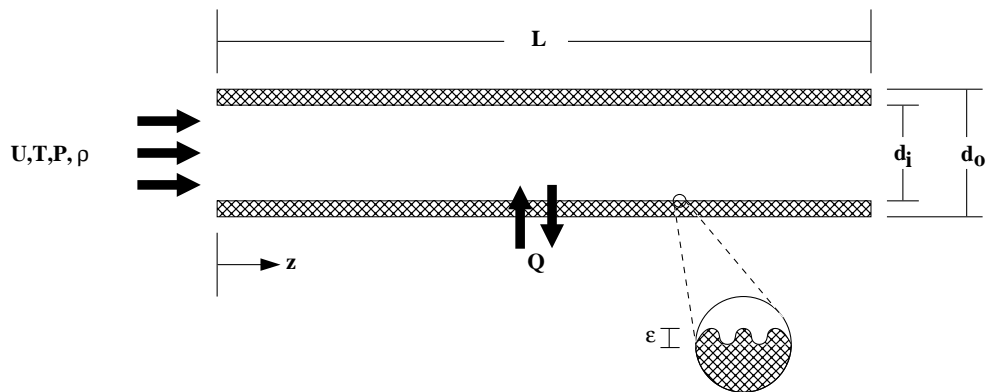
Figure 1.3: Cross Section of Capillary Tube

and local temperature values [66]. The expansion of a fluid through a capillary tube can be split into two categories: critical and sub-critical flow. Critical flow occurs when the pressure ratio from the inlet to the outlet of the capillary is sufficiently large enough to cause a Mach 1—or choked—outlet condition. Once the critical pressure ratio is reached, further reduction of the outlet pressure will have no effect on the flow conditions within the capillary [92]. The location of the choke point is dictated by the mass flow rate within the capillary tube. As a result, a sufficiently long capillary tube with a given initial mass flow rate will have a choke point that occurs before the outlet. When this occurs, the mass flow rate will decrease, moving to a different Fanno line such that the choke point occurs at the outlet. Sub-critical flow occurs when lower pressure ratios are present and the choke point for the flow would occur past the outlet of the capillary.
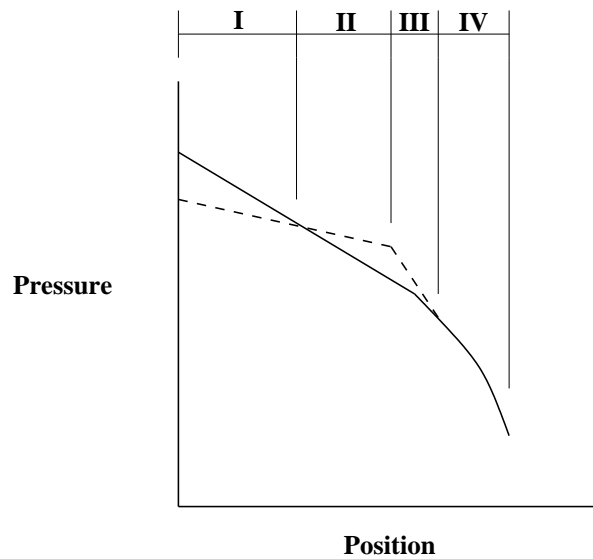
Figure 1.4: General capillary flow with pressure (-) and saturation pressure (- -) curves. (**I**) Single-phase subcooled region; (**II**) Metastable single-phase liquid region; (**III**) Metastable two-phase liquid-vapor region; (**IV**) Thermodynamic equilibrium two-phase liquid-vapor region

The expansion of a supercritical fluid and subsequent reduction in pressure along the capillary tube causes the fluid to undergo a flashing process, where the pressure is

5
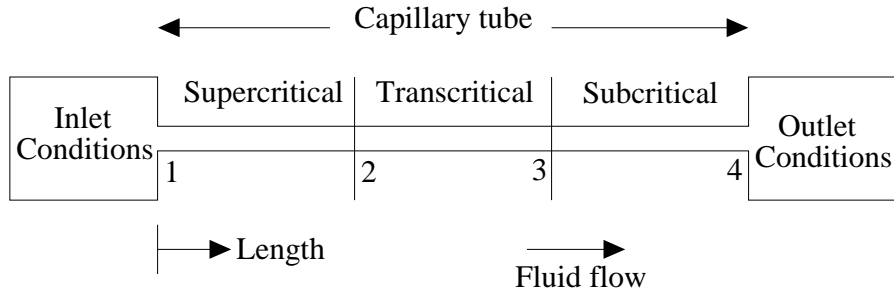
Figure 1.5: Flow Regions within an Adiabatic Capillary Tube, adapted from Agrawal et al. [4]

reduced below the vapor pressure and condensation occurs. It was originally believed that only two flow regimes existed within the framework of the capillary expansion device (experiments by Bolstad and Jordan [10] identified only a single-phase and a two-phase flow region). However, it was later deduced through experiments by Mikol [62], Li et al. [47], and Lin et al. [50] that there is a metastable region between the single-phase and two-phase regions. A metastable flow occurs when the system is not in thermodynamic equilibrium, delaying the vaporization of the working fluid [4]. The flashing point is delayed such that the pressure of the flow is decreased below the equilibrium saturation pressure before vaporization occurs, as shown in Figure 1.4 [4].

The flow regimes present in a typical capillary tube are illustrated in Figure 1.5, where the metastable regions (II and III in Figure 1.4) occur in the transcritical region of the fluid, near the saturated line of the vapor dome. The subcritical flow occurs once the flow transitions to two phases within the vapor dome. In order to idealize the process, it is typically assumed that the metastable region is negligible, resulting in a flow that is in thermodynamic equilibrium everywhere, shown in Figure 1.6, where locations 1 and 4 refer to the locations in Figure 1.5. Due to this idealization, non-equilibrium modeling can be ignored and the spinodal curve can be neglected. The spinodal curve is a line in the two-phase region that, when crossed by a metastable

fluid, forces the fluid into thermodynamic equilibrium. Since the metastable region is neglected, the spinodal is also neglected.
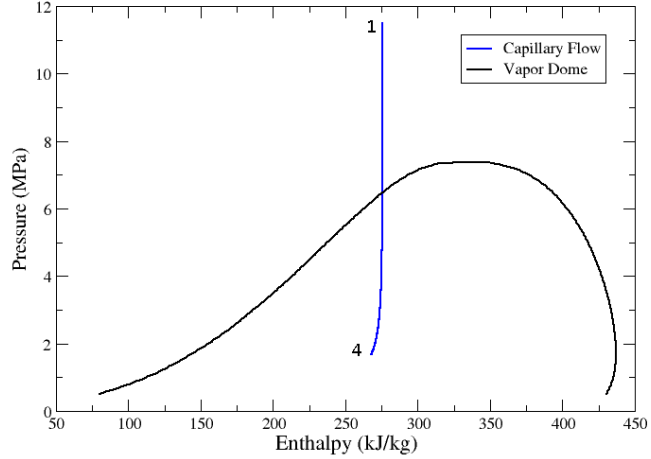
Figure 1.6: Pressure-Enthalpy diagram of a typical adiabatic capillary

1.1.2 Expansion Chamber

The supersonic and subsonic free jet regions, sections IV and V, are situated within the expansion chamber of the RESS process. At the outlet of the capillary tube, point c in Figure 1.2, the flow is underexpanded with a Mach number of unity. The difference in pressure between the capillary exit and the expansion chamber will cause the flow to rapidly expand to a point where it is over-expanded to a pressure much less than the expansion chamber. The result is a normal shock that nearly instantaneously increases the pressure of the flow to the conditions of the expansion chamber and forms what is called a Mach disk, given by point d. Figure 1.7 shows a two-dimensional simulation of the expansion of CO_2 at the exit of the capillary tube. The high pressure is shown to be at the capillary exit, which then expands in a conical shape, called a Mach cone, to the over-expanded pressure. The occurrence of

7
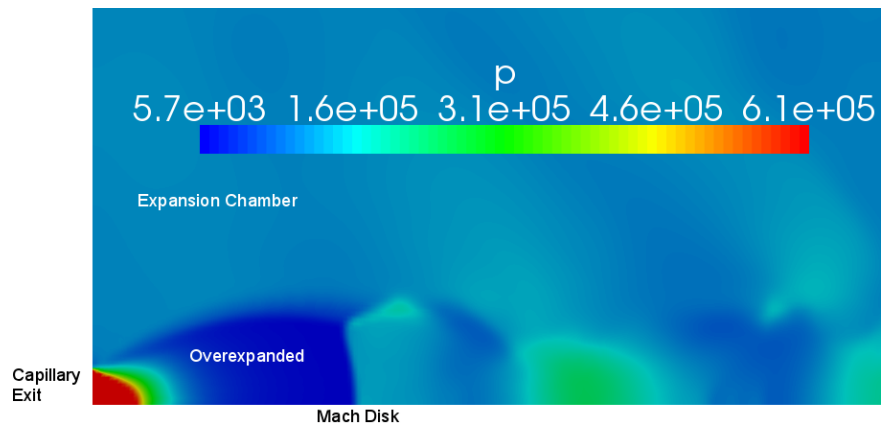
Figure 1.7: Expansion chamber simulation for CO_2 with no implementation of particle growth

the normal shock then creates the Mach disk to raise the pressure to the expansion chamber conditions.

CHAPTER 2

LITERATURE REVIEW

In order to fully investigate the previous literature, three key research threads are investigated. The first research thread focuses on capillary flows as they are commonly used within several industrial applications and there exists literature dedicated solely to their study. Secondly, a review of the RESS process and associated literature is necessary to provide an overview of where the capillary flow fits into the overall process. Lastly, the third research thread is focused on carbon dioxide and ethanol mixtures to allow for the study of the binary supercritical fluid expansion through he capillary tube.

2.1 Capillary Flow

New regulations within industry combined with a better understanding of a fluids Global Warming Potential (GWP) have encouraged research into alternative refrigerants capable of running efficiently with fewer negative impacts on the environment. This has led to two distinct aspects of capillary research. The first is focused on expanding the experimental database of refrigerants in order to find a new working fluid for popular refrigerator devices. The second aspect has been to study, both analytically and experimentally, the impact of having an adiabatic versus a non-adiabatic capillary tube. The distinction between adiabatic and non-adiabatic flows is important as there exists industrial applications for both assumptions.

Melo et al. [57] investigated adiabatic capillary tubes and the effects of geometry, degree of subcooling, and condensing pressure using CFC-12, HFC-134a, and HC-

600a as the refrigerants. They found that the diameter of the capillary has the single most effect on the mass flow rate and that the effect of the length on the mass flow rate is independent of the subcooling and condensing pressure. da Silva et al. [19] provided a similar adiabatic analysis to Melo et al. [57] using CO_2 as the refrigerant.

Hermes et al. [38] provided an extensive experimental investigation of both adiabatic and non-adiabatic capillary tubes. They used several refrigerants, including CFC-12, HCFC-22, HFC-134a, HC-600a, R-404A, R-407C, and R-507A for adiabatic flows and HFC-134a and HC-600a for non-adiabatic flows with concentric and lateral capillary tube–suction line heat exchanger configurations. Melo et al. [59] provided a similar non-adiabatic analysis as Hermes et al. [38] for HC-600a, which highlighted the efficiency of a program called CAPHEAT.

To complement the experiments conducted in the literature, several authors have developed methods to model the adiabatic flow in capillary tubes. While multiple phases are present in a capillary tube expansion device, it is common to assume that the two phases act as one homogenous fluid. Agrawal and Bhattacharyya [4] studied the homogenous flow assumption by comparing to another method called the separated flow method. The separated flow method treats the two phases separately within the capillary in order to take into account the higher velocity vapor. This study showed that the separated and homogenous flow models each represent the flow conditions within an acceptable margin of error and that the assumption of homogenous flow is valid under the conditions investigated. Similar to the separated flow model, Liang and Wong [48] used the two-phase drift flux model, which includes the slip velocities while solving the mixture conservation equations in order to take into account the two phases while not treating them separately. Using R134a as the working fluid they compared their method to experimental results and determined it is a valid method, but did not elaborate on any improvement over previously established methods.

Lin et al. [50] used the homogenous flow assumption to illustrate that the Churchill equation [16] for the single-phase friction factor and a multiplier for the two-phase region used by Lockhart and Martinelli [51] matched experimental results. Bansal and Rupasinghe [6] incorporated these frictions factors into a program called CAPIL, which studies the performance of adiabatic capillary tubes in small vapor compression refrigeration systems using the Reference Fluid Thermodynamic and Transport Properties Database (REFPROP) as the equation of state [46]. The accuracy of the CAPIL simulations when compared to experiments was found to be approximately $\pm$ 10%. Wongwises and Pirompak [86] expanded upon the program CAPIL to create a program that could be used for several different refrigerants and two-phase viscosity models. The Dukler [24], McAdams [54], Lin [50], and Cicchitti [17] viscosity models were found to be acceptable, but no one model was universally better for all refrigerants. They did find that the Duckler and McAdams models had the best average discrepancies when compared to experiments.

Yilmaz and Ünal [89] created an analytical method for capillary design that can be used for many working fluids, however the method varies up to 19% from experimental results. Melo et al. [57] used dimensional analysis to create analytical correlations of the mass flow rate for various refrigerants, lengths, and diameters that are accurate to +15% and -10% compared to experiments. Sami and Maltais [71] investigated how efficient the working fluids R407, R410A, and R410B would be in a capillary expansion device by using the homogenous assumption and showing adequate correspondence with experiments. Madsen et al. [52] as well as Agrawal and Bhattacharyya [2] studied the effect of using transcritical CO_2 on refrigeration systems. They found significant pressure gradients along the capillary flow as compared to other refrigerant methods.

Bansal and Wang [7] developed a full range simulation diagram to better understand graphically the choked flow phenomenon occurring in capillary flow, shown in Figure 2.1. This figure helps establish an understanding of how flow characteristics
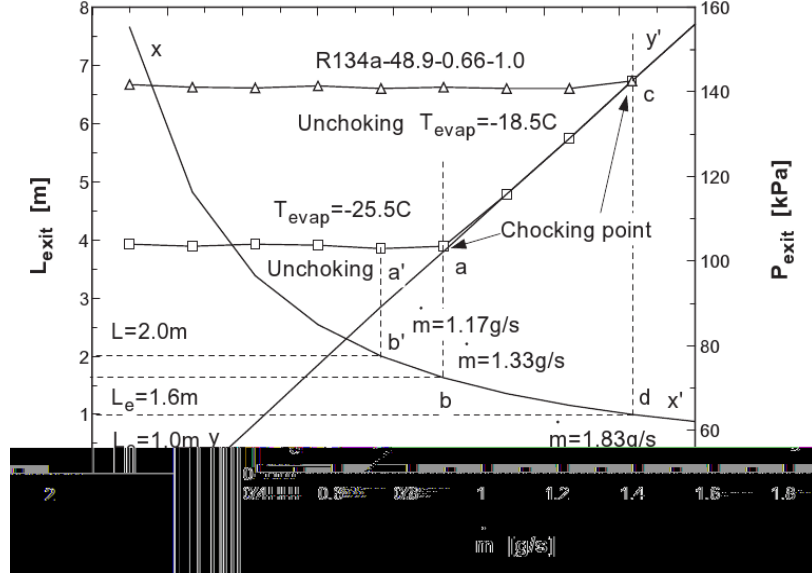
Figure 2.1: Full range diagram showing $\dot{m}$-L-P characteristics for R134a [7]

will change with a change in initial conditions. Two sets of data are shown for two different evaporator temperatures, or inlet temperature when not within a refrigeration cycle, with their corresponding choked length and mass flow rate. The initial conditions are given by the evaporator pressure and temperature, since Bansal and Wang [7] are working with capillary tubes for refrigeration cycles. If the mass flow rate for T_{evap}=-25.5 °C is lowered from a choking point (point a) with mass flow rate 1.33 g/s (point b) to a non-choking point (point a') with mass flow rate 1.17 g/s (point b') then the corresponding choked length will increase from 1.6 m to 2.0 m. The straight line passing through points a and c identifies the choking mass flow rate for a given temperature and pressure.

Models within the literature have also been expanded to include non-adiabatic flows. Garcia et al. [31, 30] determined that the best accuracy for non-adiabatic heat exchange with the surroundings can be achieved by taking into account the metastable effects and solving the general semi-integrated governing equations discretized in space for the separated flow model instead of the homogenous flow model. Xu and Bansal

[87] studied the interaction of the capillary flow with a non-adiabatic antiparallel suction line to show that the flow characteristics change depending on if the pressure drop or heat exchange is dominant. If the heat exchange is dominant, then the refrigerant tends to condense in the heat exchange region, while if the pressure drop dominates, then the refrigerant tends to flash. Agrawal and Bhattacharyya [3] used a similar geometry to confirm that flow characteristics depend on the dominance of the pressure drop or heat exchange for transcritical CO_2.

Chen and Gu [14] used the homogenous assumption to solve transcritical CO_2 capillary flow with heat exchange to the surroundings. They found that a proper relation between the capillary length and diameter must be established to minimize size and maximize efficiency. Seixlack and Barbazelli [74] quantified the improvement that the separated flow model gives over the homogenous flow model for capillary tubes with with lateral and concentric antiparallel suction lines with 3.6% and 5% relative mean error in the mass flow rate respectively. This shows that both models are acceptable, but the separated flow model is more accurate.

2.2   Rapid Expansion of Supercritical Solutions

The RESS process is not fully understood within the literature, which has led to contradicting statements between different authors [36]. Recent works have attempted to experimentally and theoretically investigate the RESS process in order to provide a greater understanding of the process, but more research is necessary. Early models attempted to minimize the solution domain by making simplifying assumptions. Kwauk and Debenedetti [45] modeled the one-dimensional aerosol formation of the RESS process using continuity, momentum, energy, and the aerosol general dynamic equation (GDE) for the capillary inlet and capillary tube while leaving the expansion chamber out of the solution. They were able to determine the nucleation rate, particle size distribution, and average solute particle size along the expansion

path. The results relied on the assumption that the coagulation effects due to Brownian motion were negligible, due to the fact that the residence time in the nozzle was much less than the characteristic coagulation time. However, the investigation into Brownian motion coagulation demonstrated that it should not be neglected when dealing with particles that vary significantly in size. The particles obtained at the exit of the capillary had size ratios that were small enough to allow the coagulation to be neglected. Further investigation was deemed necessary to study the effects of viscous dissipation and two-dimensional flow.

Ksibi and Subra [43] presented a multidimensional solution domain consisting of the nozzle, of which 3 different geometries were studied, and the expansion chamber. The solution method involved solving the Navier-Stokes equations for the flow domain, with which they were able to capture the Mach disk, followed by solving the aerosol transport model presented by Kwauk and Debenedetti [45]. Franklin et al. [28] followed a similar multidimensional decoupled approach to Ksibi and Subra [43] that is attractive due to its simplicity. This decoupled approach assumes that the fluid is homogenous due to the low concentration of the precursor and solves a separate aerosol transport equation for particle formation. The solution domain included the entire RESS process, including the capillary inlet, capillary tube, and expansion chamber. A full investigation of the effects of coagulation due to Brownian motion, mean shear, and turbulence was also included. Figure 2.2 shows that the assumption of no coagulation when the solution domain ends at the exit of the capillary, x≈0.018, could be considered valid. However, when the expansion chamber is added to the solution domain, the effects of coagulation can be seen to be significant for Brownian motion and turbulence effects. Mean shear coagulation contributes slightly to particle growth, but to a lesser extent. They found that while they were able to produce particles on the micron scale (which is comparable to experiments of Chernyak et al.
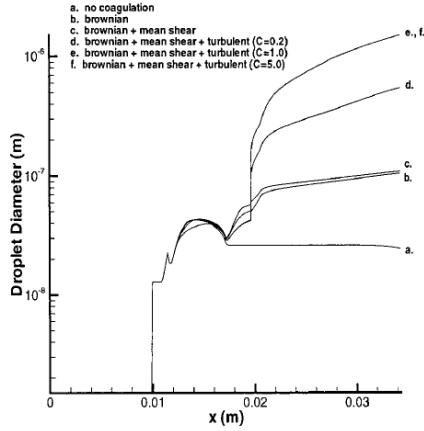
Figure 2.2: Comparison of the effects of coagulation on particle growth through the capillary tube and into the expansion chamber [28]

[15]), the calculated Sauter Mean Diameter (SMD) was consistently smaller than the experimentally found values.

Shaub et al. [75] modeled the flow into the expansion chamber as an inviscid radial flow taking into account nucleation and diffusional growth and assuming no precipitation in the nozzle. The resulting particle sizes were on the order of a micron, but could not be compared to experiments due to high pre-expansion conditions and a vacuum pressure in the expansion chamber that does not occur in experiments. Domingo et al. [22, 23] studied the experimental effects of using capillary tubes with diameters around 65 μm and the use of a porous plate nozzle, also called a frit nozzle, with diameters down to 1 μm. They determined that an adiabatic assumption is not valid for the flow through the capillary tube by experimentally measuring temperatures along the capillary and within the expansion chamber. It was also determined that the diameter of the expansion tube effects particle size. The small diameter of the frit nozzle created smaller particles than the larger diameter capillary. The small

15

diameters of the frit nozzle, however, did cause clogging in some experiments, which could potentially reduce the effectiveness of the process.

Türk [80] modeled the one-dimensional flow of the RESS process including the nozzle inlet, the non-adiabatic capillary, and the expansion chamber with the domain ending at the Mach disk. He determined that early models that use the cubic Peng-Robinson equation of state for closure are not well suited for the description of caloric data. The cubic equation of state does not accurately represent the speed of sound and the residual part of the enthalpy for the highly non-ideal, supercritical, mixture. A more accurate equation of state, such as the extended generalized Bender equation of state, was deemed necessary. Initial precipitation was found to occur due to homogenous nucleation within the capillary followed by contributions from coagulation and condensation until the flow is no longer supersaturated. Coagulation in the free-jet of the expansion chamber, up to the Mach disk, was found to dominate the particle growth. Helfgen et al. [36] modeled the same domain as Türk [80] and found that the particles at the Mach disk were on the order of a few nanometers, while experiments have shown particles should be on the micron scale. This has been used to infer that particle growth from coagulation continues past the Mach disk in the expansion chamber with the conditions of the expansion chamber significantly influencing particle growth. Further experiments by Türk et al. [79] confirmed that the expansion chamber may influence the particle growth. They experimentally produced particles on the scale of 200 nm, while theoretically they should have obtained particles 2-10 nm in size up to the Mach disk.

Weber et al. [83] modeled the subsonic region of the RESS process, which consists only of the nozzle inlet and capillary tube. They found that while late nucleation dominated particle growth, appreciable amounts of coagulation occurred within the capillary tube. At the exit of the capillary tube the particles were on the order of 5-10 nm. This signifies that the coagulation dominated transonic region of the free jet

contributes significantly to the particle growth of RESS. Helfgen et al. [37] developed a model of the entire one-dimensional RESS process starting at the nozzle inlet and ending past the Mach disk in the expansion chamber. Particle growth is modeled using the general dynamic equation for simultaneous nucleation, coagulation, and condensation. When compared to experimental results, they found that the simulation overestimated the size of the particles at the end of the expansion chamber, with the majority of particle growth occurring past the Mach disk. They concluded that a multidimensional model of the expansion chamber would be necessary to increase the accuracy, supporting a similar statement by Kwauk and Debenedetti [45].

Hirunsit et al. [39] performed a numerical analysis on a solution domain that included only the capillary nozzle and supersonic free jet for the expansion of ibuprofen with CO_2. They found the flow within the capillary to be similar to the results achieved by Weber et al. [83], but that the supersaturation, given by Equation (1.1), did not exceed a value of 3.2 until after exiting the nozzle. This indicates that precipitation of the ibuprofen would not occur until it reached the supersonic free jet, as previous studies by Weber et al. [82] showed that supersaturation ratios greater than 4 were necessary for the onset of precipitation. Particle growth by diffusion was calculated using the Stokes-Einstein equation, for which the particle diameters were found to be within the range of 1-2 μm. These results are comparable to the experimental results conducted by Charoenchaitrakool et al. [13], where the mean particle size was below 2.5 μm. The high level of accuracy is surprising due to previous studies by Franklin et al. [28] that showed that coagulation is driven by several factors where the Stokes-Einstein diffusion equation only takes into account coagulation due to Brownian motion.

In order to further understand the mechanisms of particle growth within the RESS process, Weber and Thies [84] performed a detailed study of nucleation, condensation, and coagulation separately while assuming only one mechanism was dominant at a

time with no interaction between mechanisms. A two-step process for homogenous nucleation and condensation is assumed to begin when a supersaturation ratio of 4 is reached and produces particles of a constant diameter until condensation becomes the dominant precipitation process and particle growth occurs. The supersaturation ratio of 4 was chosen due to simulations carried out by Weber et al. [82] that showed that it is the likely starting point of nucleation. The coagulation due to particle-particle interaction was assumed to begin once the solute mole fraction neared its equilibrium value. Performing a similar analysis to Franklin et al. [28], the coagulation effects due to Brownian motion, shear flow, and slip flow between the dispersed phase and continuous phase were each investigated. They found that the characteristic time, from largest to smallest, was for Brownian motion, shear flow, and slip flow respectively. These results are consistent with those of Franklin et al. [28] that found coagulation due to turbulence produced the greatest increase in particle growth followed closely by the shear flow.

Ghoreishi and Komeili [32] followed similar assumptions established by Kwauk and Debenedetti [45], but used equations established by Weber et al. [83], Weber et al. [84], and Hirunsit et al. [39] due to discrepancies found within the literature. The one-dimensional simulation of the entire RESS process took into account homogenous nucleation, condensation, and coagulation due to Brownian motion while considering the coagulation due to shear and relative motion negligible. The model was capable of accurately determining the particle growth along the expansion process with an average relative error of 6.1% , average absolute error of 3.9 nm, and a probable error of 4.8 nm. These results contradict the findings of Franklin et al. [28] that established that coagulation due to Brownian motion is not the only dominant coagulation force while also contradicting the statements of Kwauk and Debenedetti [45] and Helfgen et al. [37] that stipulated a multidimensional expansion chamber would be necessary to gain adequate accuracy.

2.3 Carbon Dioxide/Ethanol Mixtures

As the PRESS process is a new technique, no literature known to exist that studies the process directly. Therefore it is necessary to investigate the applicability of previous research to the aspects of PRESS that were not discussed within the areas of capillary flow and the RESS process. The most distinct difference is the addition of a second supercritical fluid, which has been utilized frequently due to its usefulness within the SFE process. The binary supercritical fluid has been shown to increase the yield percentage of the precursor [20, 35, 77, 40]. It also has a wide array of applications, including being used for grape seed [63], fish oil [12, 11], and caffeine product [70] extractions. In addition to increasing the effectiveness of the process, the mixture also increases the complexity of the problem. Bennett et al. [9] showed that a typical equation of state, such as the Peng-Robinson with van der Waals one-fluid mixing rules cannot accurately describe the mixture of ethanol with gasoline. This is due to the non-ideality of the mixture and extends to the addition of ethanol with CO_2.

Investigations into the properties of CO_2 and ethanol mixtures can also be applied to the flow properties of PRESS. Ziegler et al. [90] and Yeo et al. [88] experimentally studied the critical properties of supercritical fluid mixtures using independent methods, the peak-shape method and the variable-volume view cell respectively, to obtain similar results. The experimental results from Yeo et al. [88], shown in Figure 2.3, illustrates that an increase in the concentration of ethanol within the CO_2/ethanol mixture increases the critical properties. Abdulagatov et al. [1] collected data for all carbon dioxide binary mixtures established within the literature into a review paper for easy reference.

The experiments that document the interaction between the supercritical fluid mixtures are important for the development of an equation of state that is applicable to mixtures. Figure 2.4 shows experiments conducted by Secuianu et al. [73] com-
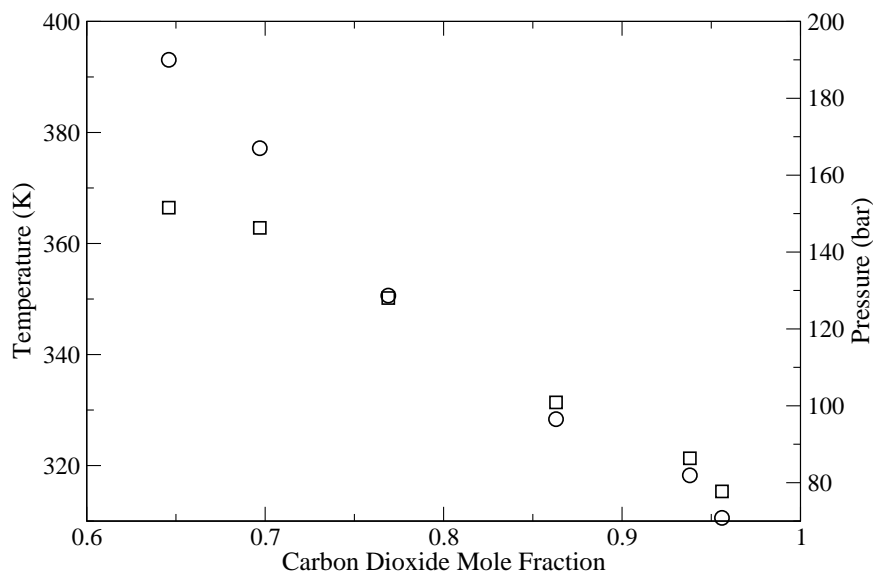
Figure 2.3: Critical temperature, $\bigcirc$, and pressure, $\square$, for various concentrations of CO_2 with ethanol from Yeo et al. [88].

pared with experiments with others from the literature for different concentrations of carbon dioxide-ethanol mixtures. It illustrates that the pressure can vary significantly depending on the concentration of the mixture for a constant temperature. Secuianu et al. [73] were able to use these experimental results to develop a cubic equation of state based upon the general cubic equation of state (GEOS) and the classical van der Waals two component mixing rules. The average absolute deviations in bubble point pressure (AADP, %) and average absolute deviations in the vapor phase compositions (AADY, %) for the carbon dioxide and ethanol system were found to be at most 6.9% and 8.6%, respectively.

An alternative method to establish an equation of state for non-ideal mixtures has been proposed by Neroorkar and Schmidt [65]. The method, called GEFlash, is intended for determining the mixing properties of a gasoline-ethanol mixture for varying levels of ethanol content. However, it can be extended beyond gasoline-ethanol blends by determining new constants for the desired mixture. GEFlash is capable
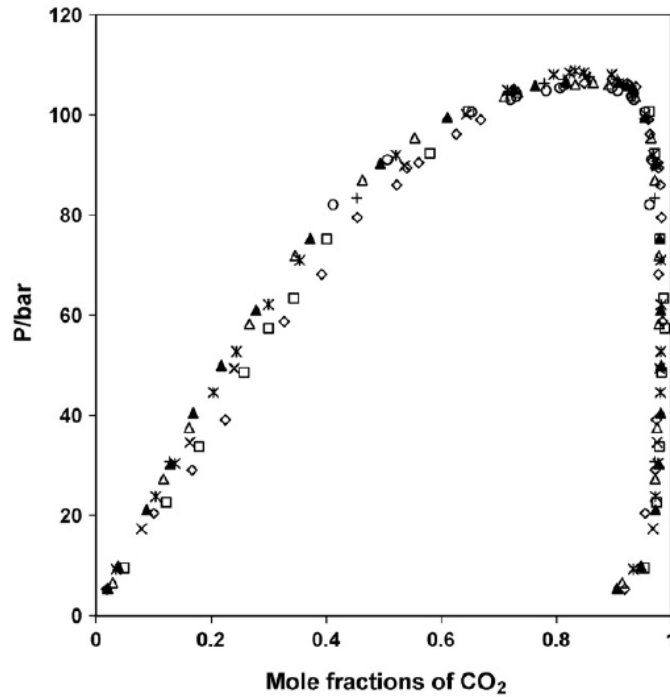
Figure 2.4: Comparison of Vapor-Liquid Equilibrium data for carbon dioxide+ethanol from Secuianu et al. [73]: ($\square$), 333.15 K, Secuianu et al. [73]; ($\circ$), 333.2 K, Lim et al. [49]; ($\diamond$), 333.27 K, Nagahama et al. [64]; ($\triangle$), 333.4 K, Joung et al. [42]; ($\blacktriangle$), 333.4 K, Suzuki et al. [76]; ($\times$), 333.53 K, Mendoza de la Cruz and Galicia-Luna [61]; ($+$), 333.75 K, Galicia-Luna et al. [29]; ($*$), 333.82 K, Galicia-Luna et al. [29]

of providing a full description of the mixture properties by combining equations of states with other vapor-liquid equilibrium methods.

CHAPTER 3

HOMOGENOUS METHOD: PURE FLUIDS

The initial step to gaining a full understanding of the binary supercritical capillary flow that occurs within the PRESS process is to understand the single component multiphase expansion within a capillary tube. The two dimensional capillary tube, shown in Figure 3.1, is assumed to be one-dimensional for this method. It has a given length, L, inner diameter, d_i, outer diameter, d_o, and surface roughness, ϵ. The flow travels in the z direction where the properties of the flow are temperature, T, pressure, P, and density, ρ, with a velocity, U. The heat transfer, Q, will be present depending upon whether an adiabatic or non-adiabatic assumption is used.

3.1 Methodology

In order to model the flow within a capillary tube, the following assumptions are made:
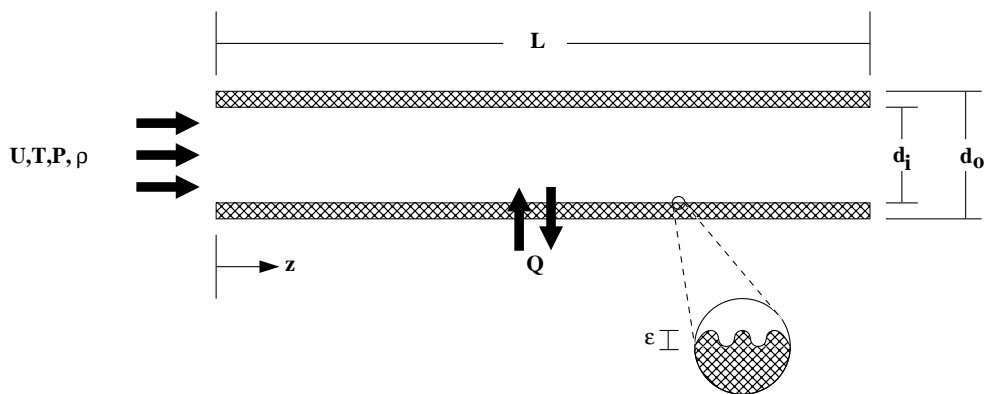
Figure 3.1: Cross Section of Capillary Tube

- One-dimensional flow in the axial direction

- Constant surface roughness within the capillary tube

- Thermodynamic equilibrium everywhere (metastable phenomenon ignored)

- Thermodynamic properties are defined by the bulk properties, via the homogenous assumption

- Steady state flow

- The single-phase and two-phase velocities are equivalent (No slip velocities)

3.1.1 Adiabatic Flow

For the case of adiabatic flow, the energy equation, Equation (3.1), can be derived using conservation of energy (shown in Appendix A.1).

$$\frac{dh}{d\rho} = \frac{g^2}{\rho^3} \tag{3.1}$$

The enthalpy and mass flux are given by h and g, respectively. The momentum equation, given by Equation (3.2), can be similarly derived from conservation of momentum (shown in Appendix A.2).

$$\frac{dz}{d\rho} = \left[\frac{g^2}{\rho^2} - \frac{dP}{d\rho}\right] \frac{2\rho d_i}{f_h g^2} \tag{3.2}$$

The hydraulic fiction factor and axial location within the capillary tube are given by f_h and z, respectively.

Typically a one-dimensional domain is easiest to discretize in space. However, Hermes et al. [38] and da Silva et al. [19] showed that discretizing with respect to pressure was more appropriate due to the stability of the flow domain. As the capillary flow reaches the outlet, $\left|\frac{dP}{dz}\right|$ goes to a finite maximum while the inverse, $\left|\frac{dz}{dP}\right|$, goes to a minimum that is approximately zero [27]. Therefore by avoiding a discretization
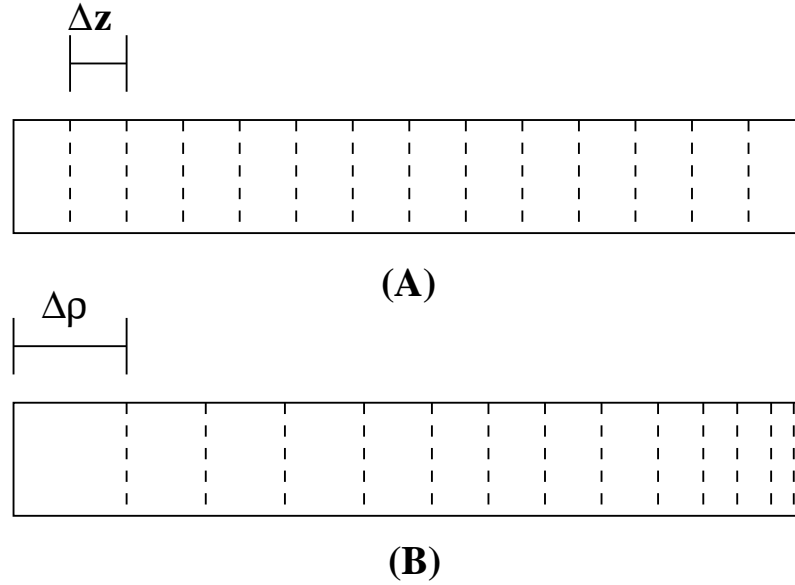
Figure 3.2: (A) Discretization with respect to z (B) Discretization with respect to ρ

in space, large derivatives can be avoided allowing for a stable solution at the outlet. Equations (3.1) and (3.2) were arranged such that they can be discretized by density in order to remove the singularity in the same fashion while allowing pressure to be the dependent variable solved for via the equation of state. It is important to note that in order to be consistent mathematically, ρ must be of the form of a monotonic function.

The benefits of discretizing by density are not limited merely to the increased stability of the system, but can also increase the accuracy of the solution. When the domain is discretized in space, the distance between each node is typically constant, however when discretized in density the distance between nodes along the capillary tube will vary depending on how quickly the density is changing. The larger the difference between the inlet and outlet densities, the more nodes will be present. Figure 3.2 shows a capillary tube that is discretized with a constant change in z, (A), and a constant change in ρ, (B). The constant change of z keeps a constant distance between nodes along the entire capillary tube, even while the properties

of the flow begin to change exponentially. In contrast, the density discretization provides a greater node concentration near the exit of the capillary tube due to the sharp density changes known to exist at the exit. With the increased node presence near the exit, the sharp changes in the properties of the flow are easier to fully capture, thus increasing the accuracy of the solution.

The hydraulic friction factor, which utilizes the Darcy friction factor, for the single-phase and two-phase regions of the capillary tube can be found using Churchill's equation [16], given by Equation (3.3).

$$f_{h,Churchill} = 8\left[\left(\frac{8}{Re}\right)^{12} + \left(A^{16} + B^{16}\right)^{-3/2}\right]^{1/12} \tag{3.3}$$

The Reynolds number, Re, is given by Equation (3.4), where μ is the viscosity.

$$Re = \frac{d_i g}{\mu} \tag{3.4}$$

The variables A and B are given by Equations (3.5) and (3.6), respectively.

$$A = 2.457\ln\left(\frac{1}{\left(\frac{7}{Re}\right)^{0.9} + 0.27\frac{\epsilon}{d_i}}\right) \tag{3.5}$$

$$B = \frac{37530}{Re} \tag{3.6}$$

The system of equations described can be solved via the method outlined in the flow chart in Figure 3.3. Given an initial pressure, temperature, and mass flow rate at the inlet of the capillary tube the simulation begins by guessing the value of the pressure at the next node. The guessed pressure value is used to solve the governing equations by numerically integrating using the first order explicit Euler method, where
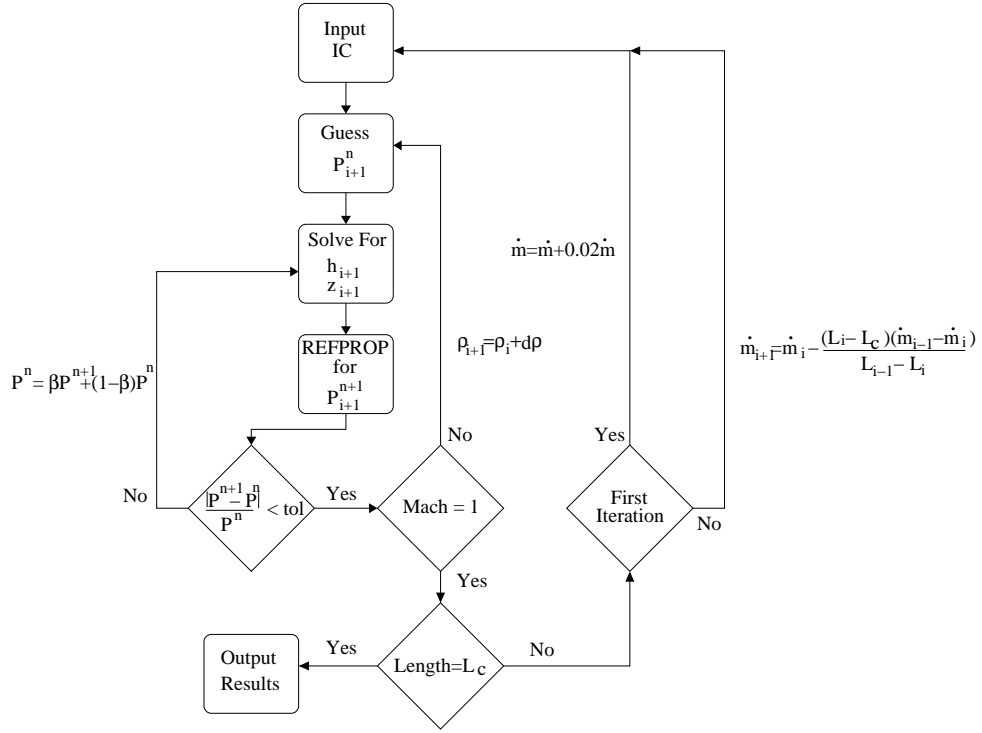
Figure 3.3: Flow Chart for Capillary Flow

Equations (3.7) and (3.8) are solved for the enthalpy and location of the next node, respectively.

$$h_{i+1} = h_i + \Delta\rho\frac{dh}{d\rho} \tag{3.7}$$

$$z_{i+1} = z_i + \Delta\rho\frac{dz}{d\rho} \tag{3.8}$$

The subscripts i and $i + 1$ designate the location of the variable for which they represent the current node and the node being calculated, respectively.

The Reference Fluid Thermodynamic and Transport Properties Database V8.0 (REFPROP) created by the National Institute of Standards and Technology (NIST) is used as the equation of state to close the system of governing equations [46]. Given two independent thermodynamic properties, such as enthalpy and density, the pro-

26

gram is capable of looking up a corresponding third property, which in this case is pressure. REFPROP can also be utilized to calculate the viscosity, thermal conductivity, specific heat, temperature, and the liquid and vapor densities of the flow when necessary.

The calculated pressure is then compared to the guessed pressure to see if a defined tolerance is reached using Equation (3.9).

$$\frac{|P^{n+1} - P^n|}{P^n} < \text{tolerance} \tag{3.9}$$

Where n and $n+1$ are the current iteration and next iteration identifiers. These are separate from the i values, as multiple iterations will occur within each discretized space. If the tolerance isn't reached, then a new pressure, P^n, is established based on on an under-relaxation of the two pressures, given in Equation (3.10),

$$P^n = \beta P^{n+1} + (1 - \beta)P^n \tag{3.10}$$

where β is the under-relaxation factor. If the tolerance is reached, then the new node needs to be checked for choked flow conditions.

The choked flow at the outlet of the capillary tube serves as the boundary condition determining when the simulation has reached a solution for a given mass flow rate. In order to enforce the boundary condition, a Mach 1 condition must exist at the outlet. It is common within the literature to determine the choking condition from the knowledge that the change in entropy, Δs, must be positive in order to be consistent with the laws of thermodynamics for Fanno flow [7]. Therefore when Δs becomes negative, it is known that the choked flow condition is present. However, a generalized method that can be applied to non-adiabatic flows is desired. For non-adiabatic flows, Δs is likely to become negative before the choking condition exists due to heat transfer and therefore is not a suitable method [8]. Since the entropy method cannot

be generalized for both adiabatic and non-adiabatic flows, a speed of sound equation can be utilized to determine the Mach 1 condition. In the single phase region the REFPROP database is capable of reporting the speed of sound, but in the two phase region the speed of sound is found using Equation (3.11).

$$w = \sqrt{\frac{\partial P}{\partial \rho}\Bigg)_s} \tag{3.11}$$

Through the use of the homogenous flow assumption the overall pressure and density change can be used within Equation (3.11) to find an accurate two phase speed of sound. For the adiabatic case it was found to approximately agree with $\Delta s > 0$ condition used within the literature.

If the flow has not reached choked conditions, then the simulation will calculate the next node by stepping by density, given by Equation (3.12).

$$\rho = \rho + \Delta \rho \tag{3.12}$$

Once the flow has reached the choked condition, then it must be determined if the desired length of the capillary tube has been established. If the desired length has not been met, then the simulation will use a root finding secant method to calculate the required mass flow rate to get the correct capillary tube length. The secant method requires two points in order to perform root finding, therefore if the first mass flow rate is not correct then the simulation will perturb the original mass flow rate, $\dot{m}$, to get a second solution by using Equation (3.13).

$$\dot{m} = \dot{m} + 0.02\dot{m} \tag{3.13}$$

Once a second loop through the simulation has occurred, then the secant method can be used to calculate the next mass flow rate, given by Equation (3.14).

$$\dot{m}_{j+1} = \dot{m}_j - \frac{(L_j - L_c)(\dot{m}_{j-1} - \dot{m}_j)}{L_{j-1} - L_j} \qquad (3.14)$$

The subscripts $j - 1$ and j represent the values from the previous two simulations, $j + 1$ represents the next simulation, and c represents the desired value. Once the correct capillary tube length is established, then the simulation is finished and the results are stored in an output file.

3.2   Homogenous Flow Results

The first step for validation is to investigate the flow within the capillary tube in the region of flow where the ideal gas laws are valid. This type of flow occurs in the vapor region of the fluid and is a single phase expansion process. In order to perform the comparison the ideal gas equation of state is substituted in for the program REFPROP. The results, shown in Figure 3.4, show that the flow along the capillary tube within the vapor region for carbon dioxide for both the presented method and the ideal gas method produce identical results.

With the simple ideal gas case validated for use within this method, the next step is to validate the two-phase flow that occurs within the capillary tube. A set of 66 simulations were performed using carbon dioxide in accordance with the experiments conducted by da Silva et al. [19], where the data for each trial are given in Appendix A.3. The simulations are able to show that the described method performs well across the set of experiments, shown in Figure 3.5, with a mean error of 8.13%.

Proprietary data of capillary expansion experiments has been provided by Melo et al. [57, 60] for isobutane and R-134a, a representative set of data is listed in Appendix A.3. Figure 3.6 shows the mass flow rate errors for the set of 189 isobutane experiments while Figure 3.7 shows the mass flow rate errors for the set of 572 R-134a experiments. The mean errors are 5.4% and 8.55% for isobutane and R-134a, respectively.
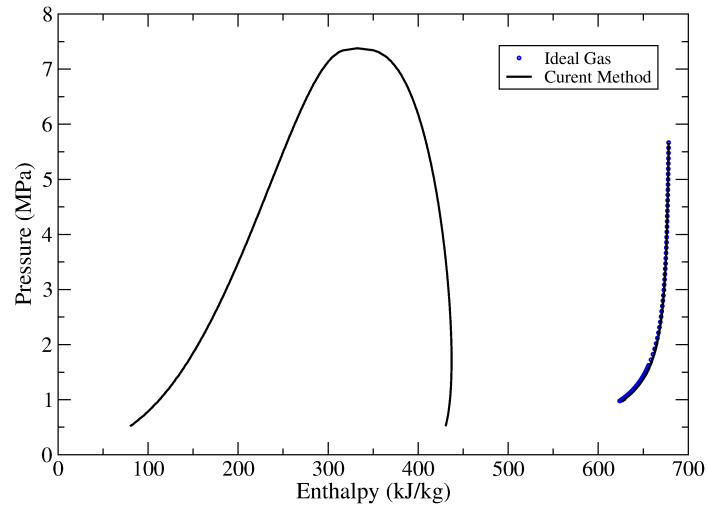
Figure 3.4: Adiabatic Capillary flow of presented model for CO_2 compared with that of an ideal gas assumption
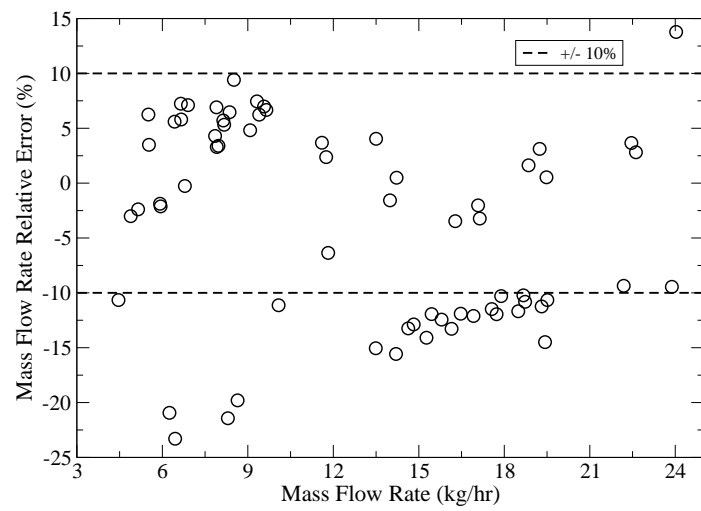
Figure 3.5: Comparison of calculated mass flow rates to experiments performed by da Silva et al. [19] for carbon dioxide
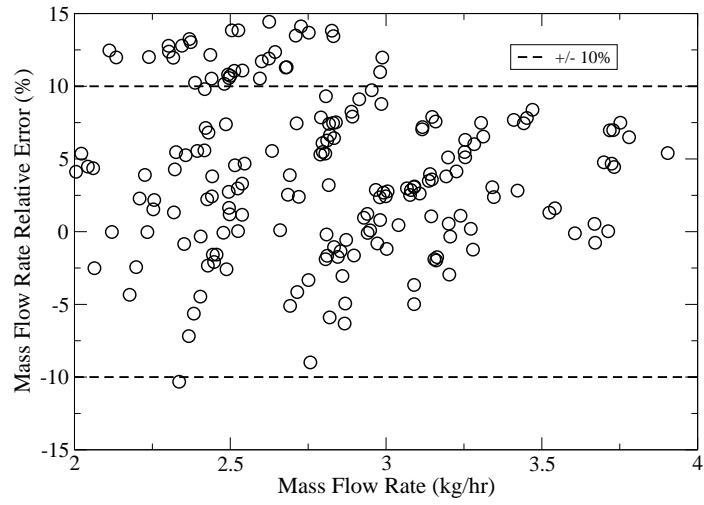
Figure 3.6: Comparison of calculated mass flow rate errors to experiments performed by Melo et al. [57] for isobutane
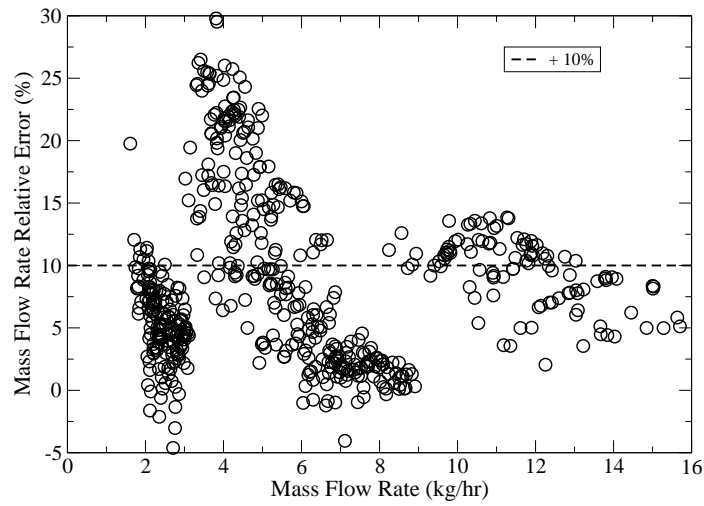
Figure 3.7: Comparison of calculated mass flow rate errors to experiments performed by Melo et al. [57] for R-134a

31
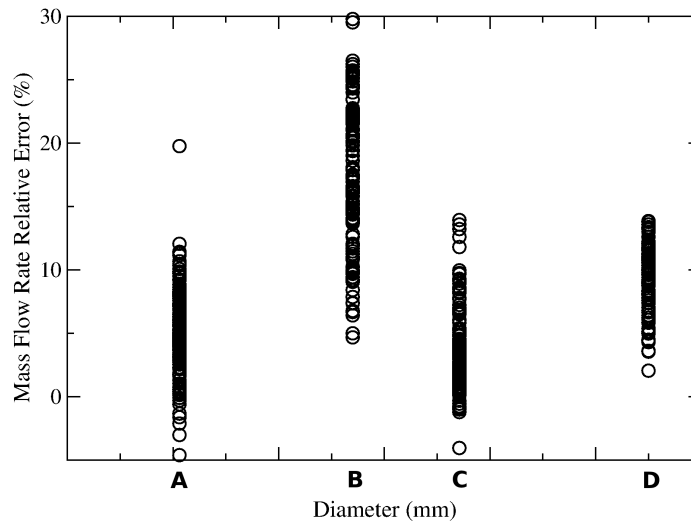
Figure 3.8: Mass flow rate relative errors compared to capillary tube diameters for experiments by Melo et al. [57] for R-134a

It can be seen in Figure 3.7 that there appears to be a trend of low accuracy results between 3 and 6 kg/hr for the R-134a simulations. This region of increased error is associated with 2, out of 6, capillary tubes that utilize a certain diameter. Figure 3.8 shows the relative error of the simulations compared to the diameters of the capillary tubes, which for proprietary reasons does not contain axis labels. Small errors associated with the measurement of the diameter and roughness of the capillary tube in experiments can be propagated into the simulations and therefore increase, or decrease, the accuracy of the model. To assess sensitivity of geometric inputs, one simulation was modified by decreasing the diameter by 0.01 mm, for which the mass flow rate decreased from 4.257 kg/hr to 4.114 kg/hr or an increase of 4% in terms of accuracy. Furthermore, a similar increase in the roughness by 0.3 μm can decrease the mass flow rate from 4.257 kg/hr to 4.185 kg/hr or an increase of 2% in terms of accuracy. By slightly varying the diameter and roughness of the capillary tube, it is demonstrated that the two parameters contribute significantly to the accuracy of the final solution.
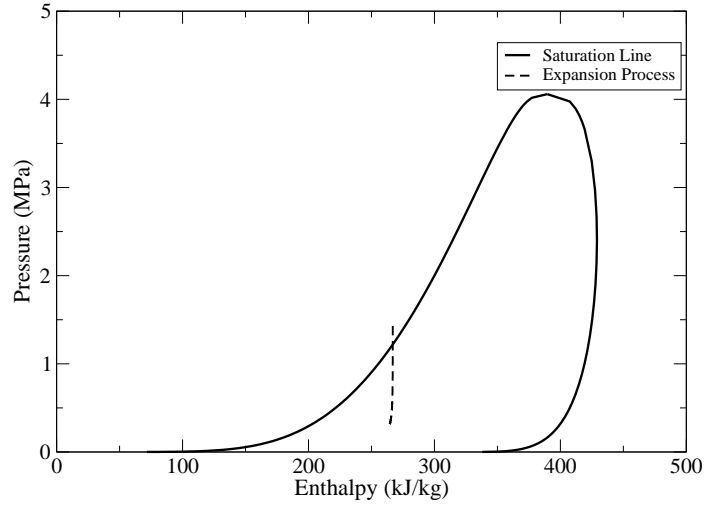
Figure 3.9: Adiabatic expansion process along capillary tube for R-134a

3.3   Homogenous Flow Assumption Conclusions

While the results of the adiabatic capillary tube simulations were impressive with regard to the mean errors, there still exists errors that should be investigated. Figures 3.9, 3.10, and 3.11 show the expansion path of 3 unique data points on a p-h diagram for R-134a, Isobutane, and carbon dioxide, respectively. Under the homogenous assumption, which is valid outside of the vapor dome, the two-phase region contains errors associated with the assumption that the vapor and liquid phases are not interacting. All of the simulations spend a significant amount of time within the two-phase region. Therefore, a method that accounts for phase interactions should be utilized for increased accuracy within the two-phase region.
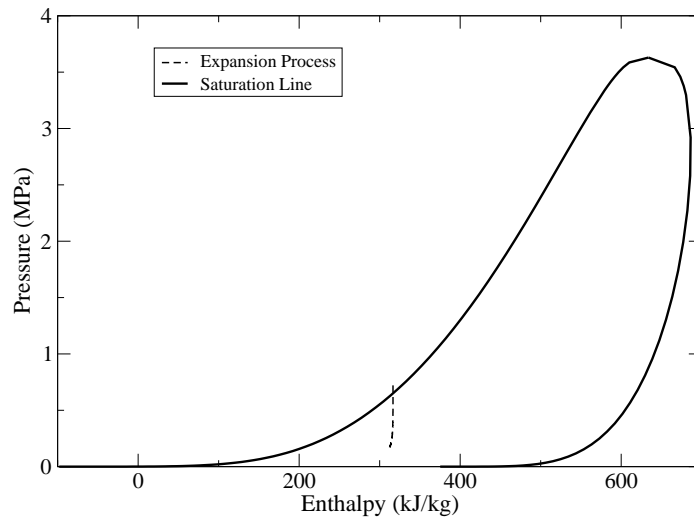
Figure 3.10: Adiabatic expansion process along capillary tube for Isobutane
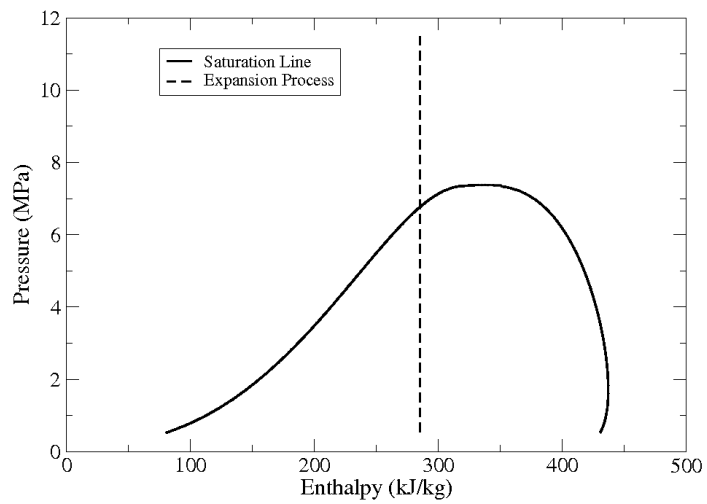
Figure 3.11: Adiabatic expansion process along capillary tube for carbon dioxide

CHAPTER 4

SEPARATED FLOW METHOD: PURE FLUIDS

4.1 Adiabatic Flow

For the single phase region, Equations (3.1) and (3.2) used previously are valid. However, Equation (3.2) is rearranged to be associated with a spacial discretization to form Equation (4.1).

$$dP = \frac{g^2}{2\rho}\frac{f_h \Delta z}{d_i} + g^2 d\left(\frac{1}{\rho}\right) \tag{4.1}$$

Within the two phase region, the method outlined by Seixlack and Barbazelli [74] is utilized. Mass conservation is given in Equation (4.2).

$$\frac{d}{dz}\left[(1-\alpha)\rho_l V_l + \alpha\rho_v V_v\right] = 0 \tag{4.2}$$

V and ρ are the velocity and density of the liquid, l, and vapor, v, components and α is the void fraction. The momentum equation for the liquid and vapor phases are given by Equations (4.3) and (4.4), respectively.

$$\frac{d}{dz}\left[(1-\alpha)\rho_l V_l^2\right] = -(1-\alpha)\frac{dP}{dz} - F_{Wl} + F_{lv} + \Gamma_l V_i \tag{4.3}$$

$$\frac{d}{dz}\left[\alpha\rho_v V_v^2\right] = -\alpha\frac{dP}{dz} - F_{Wv} - F_{lv} + \Gamma_v V_i \tag{4.4}$$

35

Where, F_{Wk} is wall friction for the component k, F_{lv} is the vapor liquid interaction term, and Γ_k is given by Equation (4.5) for the component k.

$$\Gamma_k = \frac{d}{dz}\left[\alpha_k \rho_k V_k\right] \tag{4.5}$$

The interfacial velocity, V_i, is given by Equation (4.6), where the weighting factor η is taken to be 0.5 as proposed by Wallis [81].

$$V_i = \eta V_l + (1 - \eta)V_v \tag{4.6}$$

The mixture energy equation is given by (4.7).

$$\frac{d}{dz}\left[(1-\alpha)\rho_l V_l \left(h_l + \frac{V_l^2}{2}\right) + \alpha \rho_v V_v \left(h_v + \frac{V_v^2}{2}\right)\right] = 0 \tag{4.7}$$

4.1.1 Wall Friction

For bubble and churn flow, $\alpha < 0.8$, Equations (4.8) and (4.9) are used to solve for the wall friction for the liquid and vapor regions, respectively [74].

$$F_{Wl} = \frac{(1-\alpha)f_l \rho_l V_l^2}{2d_i} \tag{4.8}$$

$$F_{Wv} = \frac{\alpha f_v \rho_v V_v^2}{2d_i} \tag{4.9}$$

The liquid and vapor friction factors, f_l and f_v, are calculated using the Churchill equation, Equation (3.3) using the Reynolds number of the liquid and vapor phases given in Equations (4.10) and (4.11), respectively.

$$Re_l = \frac{(1-\alpha)\rho_l V_l d_i}{\mu_l} \tag{4.10}$$

36

$$\mathrm{Re_v} = \frac{\alpha \rho_v V_v d_i}{\mu_v} \tag{4.11}$$

Within the annular region, $\alpha \geq 0.8$, the liquid wall friction is given by Equation (4.12).

$$F_{Wl} = \frac{f_{tp} g^2}{2 \rho_m d_i} - F_{Wv} \tag{4.12}$$

Where f_{tp} is given by the correlation of Erth [25], Equation (4.13), and since the vapor phase is assumed to in the center of the capillary there are no wall effects, ie $F_{Wv} = 0$.

$$f_{tp} = \frac{3.1}{\sqrt{\mathrm{Re_l}}} \exp\left(1 - \frac{S^{0.25}}{2.4}\right) \tag{4.13}$$

Where S is a value between 0 and 1 and represents the amount of slip between the vapor and liquid phases. Taken to be 1 for this analysis.

4.1.2 Interfacial Force

For the bubble and churn flow region the interfacial force can be calculated using the method outlined by Ishii and Hibiki [41]. The total interfacial shear force can be represented as the sum of two forces, as shown in Equation (4.14).

$$F_{lv} = \langle M_{ik} - \nabla \alpha_k \cdot \tau_i \rangle_z \tag{4.14}$$

The first term represents the average drag, while the second term models the effect of interfacial shear. The average drag can be approximated via Equation (4.15),

$$\langle M_{id} \rangle_z = -\frac{3}{4} \frac{C_D}{d_i} \alpha_d \rho_c V_r |V_r| \tag{4.15}$$

where ρ_c is the density of the continuous phase and α_d is the average overall void fraction, which in the case of one-dimensional flow simplifies to the void fraction at

the current location. It is assumed that the local relative velocity, V_r, is comparatively uniform across the capillary tube and that the magnitude of the relative velocity is smaller than both of the phase velocities. The local relative velocity is defined by Equation (4.16),

$$V_r = V_d - V_c \tag{4.16}$$

where V_d is the velocity of the dispersed phase and V_c is the velocity of the continuous phase. The drag coefficient, C_D, is calculated using Equation (4.17) [41].

$$C_D = \frac{24(1 + 0.1\mathrm{Re}^{0.75})}{\mathrm{Re}} \tag{4.17}$$

The Reynolds number is found using Equation (4.18).

$$\mathrm{Re} = \frac{\mathrm{d_i}\rho_\mathrm{l}V_\mathrm{r}}{\mu} \tag{4.18}$$

The interfacial shear force term can be calculated via Equation (4.19) [41].

$$\langle -\nabla\alpha_k \cdot \tau \rangle_z = \frac{f_i}{2}\frac{\xi_i}{A}\rho_g V_r|V_r| \tag{4.19}$$

Where f_i is found using the Wallis correlation, which is applicable for rough wavy films, given by Equation (4.20) [41, 81].

$$f_i = 0.005[1 + 75(1 - \alpha)] \tag{4.20}$$

The wetted perimeter, ξ_i, divided by the area, A, simplifies to $\frac{4}{d_i}$, resulting in Equation (4.21) for the interfacial force in the bubble and churn flow region.

$$F_{lv} = \frac{2f_i}{d_i}\rho_g V_r|V_r| - \frac{3}{4}\frac{C_D}{d_i}\alpha_d\rho_c V_r|V_r| \tag{4.21}$$

It can be seen that the first term accounts for the interfacial forces, while the second term accounts for the drag of the dispersed vapor particles traveling through the capillary tube. The annular flow region is dominated by the interfacial forces and therefore Equation (4.21) is reduced to Equation (4.22).

$$F_{lv} = \frac{2f_i}{d_i} \rho_g V_r |V_r| \qquad (4.22)$$

4.1.3   Solution Methodology

The solution method outlined for the homogenous assumption is utilized for the single phase region. Once the flow reaches the two-phase region, a Gaussian matrix solver is utilized to solve Equations (4.2), (4.3), (4.4), and (4.7) for $\frac{dV_l}{dz}$, $\frac{dP}{dz}$, $\frac{dV_v}{dz}$, and $\frac{d\alpha}{dz}$, respectively. The matrix that is solved is shown in Appendix A.4. An explicit Euler method is then utilized to find the value of the variable at the new node. The Fauske criterion [27] is utilized to determine when the choked flow condition exits, which states that at the critical point, the change in pressure $\frac{dP}{dz}$ has reached a finite maximum. This is implemented by iterating in the z-direction until $\frac{dP}{dz}$ becomes positive. Once the choked flow condition is reached, a similar root finding method is implemented to determine the mass flow rate required for the desired capillary tube length.

4.2   Separated Flow Results

Utilizing the same set of data as the homogenous flow method results in Figures 4.1, 4.2, and 4.3, which show the mass flow rate errors for carbon dioxide, R-134a, and isobutane, respectively. The mean errors are 8.03%, 5.55%, and 4.57% for carbon dioxide, R-134a, and isobutane, respectively.

It should be noted that the set of carbon dioxide simulations was reduced by one for this method as one data point was unstable for any under-relaxation factor
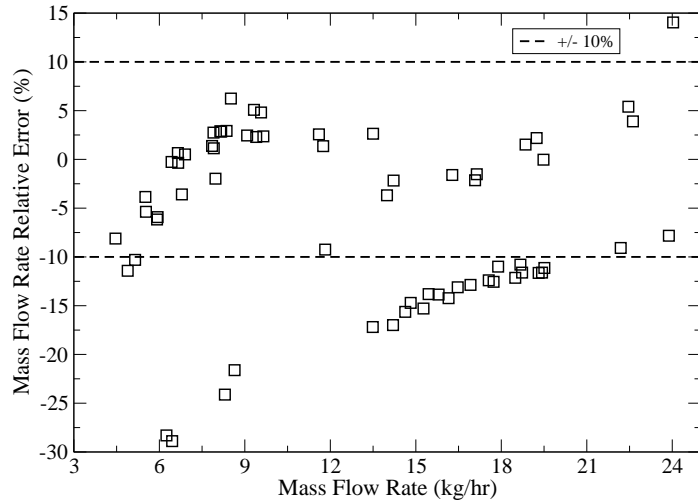
Figure 4.1: Comparison of calculated mass flow rate errors to experiments performed by da Silva et al. [19] for carbon dioxide

and resolution. It is assumed that the problem stems from the expansion process passing too near the critical point. Figure 4.4 shows the initial conditions for all of the experimental data collected by da Silva et al. [19], which shows one data point very near the critical point. Regions near the critical point tend to have increased errors in methods involving the estimation of thermophysical properties and these increased errors have the potential for causing a simulation to become unstable.
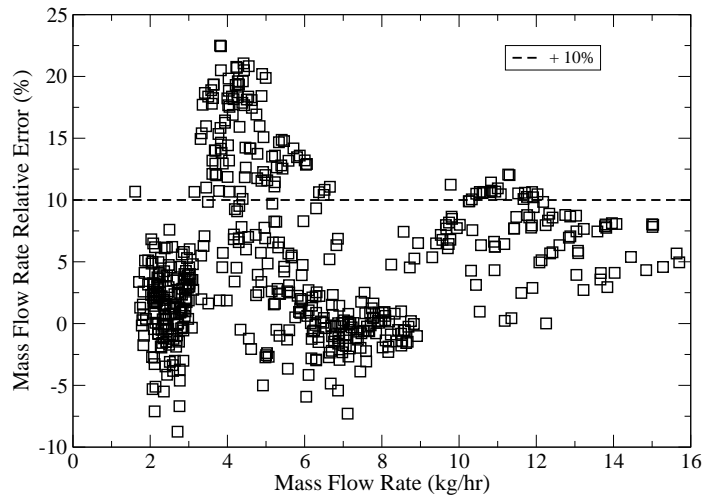
Figure 4.2: Comparison of calculated mass flow rate errors to experiments performed by Melo et al. [57] for R-134a
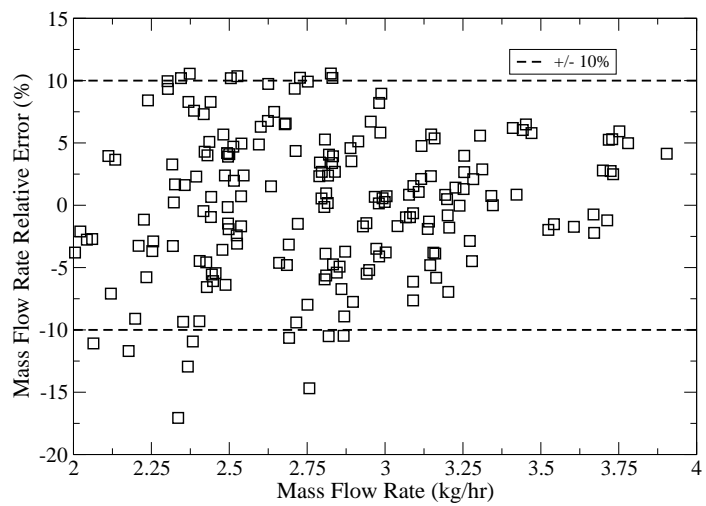
Figure 4.3: Comparison of calculated mass flow rate errors to experiments performed by Melo et al. [57] for Isobutane
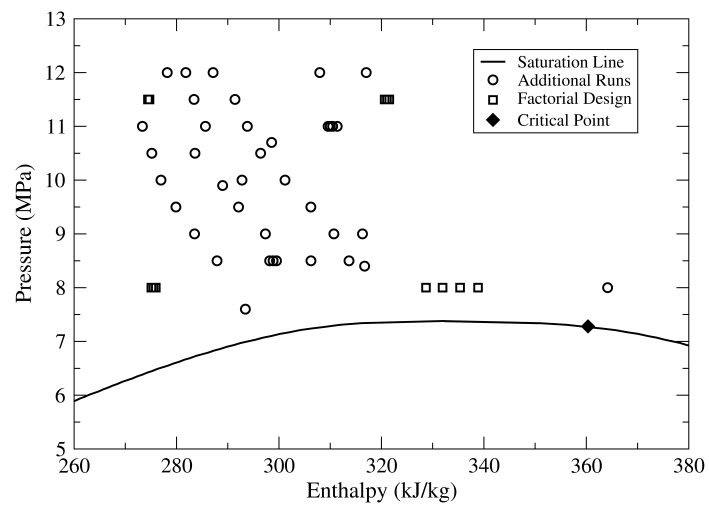
Figure 4.4: Initial conditions for experiments performed by da Silva et al. [19] using carbon dioxide

4.3 Analysis of Homogenous vs Separated Flow Methods

García-Valladares et al. [31, 30] has performed simulations using seven different methods for 8 experimental cases conducted by Melo et al. [58], shown in Table 4.1, that can be utilized as a comparison to the presented homogenous and separated flow methods. Both of the presented methods compared similarly with the simulations of García-Valladares et al. [31, 30], in particular the separated flow method is nearly as accurate as their most accurate method, method (IV). While the homogenous flow method does not perform as well as the separated flow methods, it is comparable to the homogenous flow methods from García-Valladares et al. [31, 30] and, in particular, has a lower mean error than method (VI).

It would be easy to assume based upon the mean errors presented, for both the homogenous and separated flow methods, that the separated flow method is more accurate due to a smaller mean error. However it is important to look at the statistics of the simulations to see how the two methods relate. Figures 4.5, 4.6, 4.7, 4.8, and 4.9 show the histograms for R-134a and Isobutane separated into a different histogram for each diameter of capillary tube. As the diameter utilized as the parameter to distinguish different sets of data as it is the most influential parameter on the mass flow rate [19]. It should be noted that these histograms do not appear to be Gaussian in nature, nor do they have a mean of zero, which for a perfect method would be expected. The goal of this analysis is not to prove that the presented homogenous and separated flow methods are perfect, but rather that the separated flow method out performs the homogenous method. The histograms shown in Figures 4.5 to 4.9 exhibits a trend in which the distribution of errors tends to move closer to zero for the separated flow method. Furthermore, the Kolmogorov-Smirnov and Wilcoxon Rank Sum tests, which are designed for nonparametric and non-normal distributions, were performed to test the distributions for the homogenous and separated flow methods

Case	(I)	(II)	(III)	(IV)	(V)	(VI)	(VII)	Homogenous	Separated
1	2.65	-1.35	-2.00	-4.17	-9.51	-18.71	-7.94	6.05	1.20
2	1.55	-0.25	-0.49	-1.05	-2.07	-7.49	-3.02	2.66	0.31
3	9.56	5.39	4.62	1.92	-1.84	-15.52	-1.06	12.09	5.08
4	9.18	7.15	6.84	6.03	5.52	-2.27	4.06	9.91	6.88
5	5.81	2.19	1.61	0.00	-2.52	-14.73	-4.02	7.55	1.69
6	10.21	8.58	8.36	8.40	8.08	1.84	5.59	10.19	8.08
7	4.60	1.15	0.48	-1.28	-2.33	-17.66	-5.04	5.44	0.30
8	7.08	5.45	5.17	4.90	4.77	-2.72	2.34	6.73	4.81
Mean	6.33	3.94	3.70	3.51	4.58	10.12	4.13	7.58	3.54

Table 4.1: Mass flow rate relative error (%) for presented homogenous and separated flow methods compared to methods found in García-Valladares et al. [31, 30] using isobutane as the working fluid. Models (I), (II), and (III) utilize a homogenous method while (IV), (V), and (VI) utilize a separated flow method. Model (VII) does not consider the metastable region.
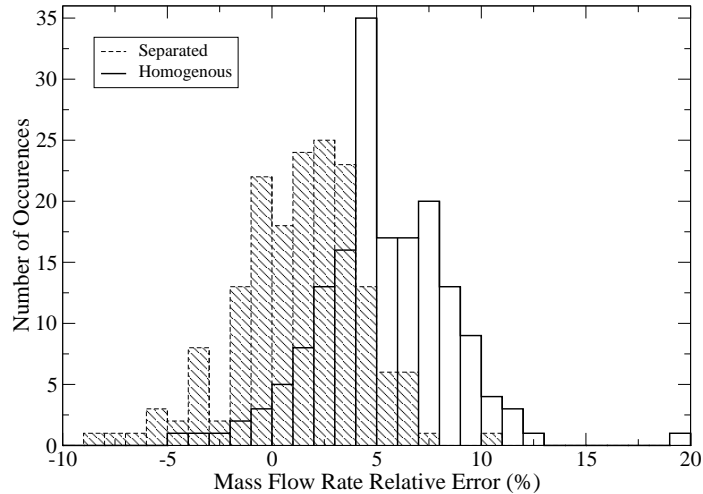
Figure 4.5: Homogenous and separated flow method histograms for R-134a data provided by Melo et al. [57] for diameter A (from Figure 4.10)

were statistically and significantly different. For a 95% confidence level the tests determined that the two methods are statistically and significantly different.

To further analyze the results of the homogenous and separated flow methods it can be seen in Figures 3.8 and Figure 4.10 that the accuracy of the solution can be correlated to the diameter of the capillary tube. As previously discussed, small errors associated with the measurement of the capillary tube diameter can have a significant effect on the accuracy of the simulation. To exemplify the sensitivity of the simulations to measured quantities, the simulations for R-134a were repeated for a roughness equivalent to that of capillary tube A using the homogenous flow method. For clarity, the two sets of data are shown slightly offset in Figure 4.11, but note that these simulations do not actually represent different diameter capillary tubes. It can be seen that the small change in roughness causes the range of accuracies for each of the capillary tubes to shift by several percent in the same direction. All three accuracy ranges shift in the same direction due to the fact that the roughness of capillary tubes B, C, and D are all smaller than A. If the roughness of one of the capillary tubes was larger than A, then the range of accuracy would trend in the

45
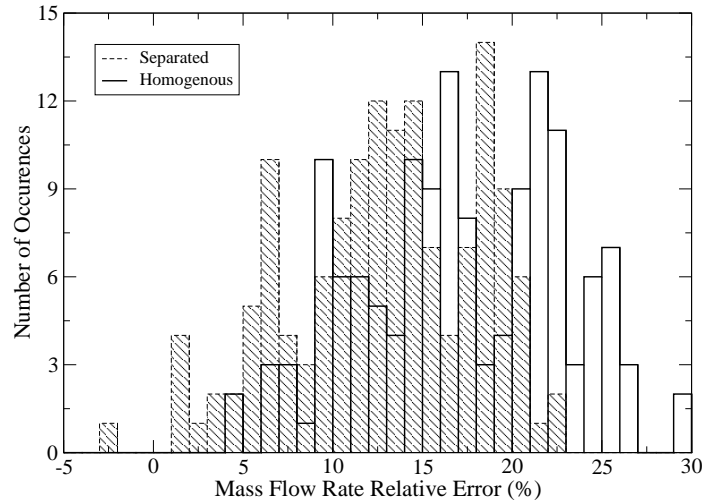
Figure 4.6: Homogenous and separated flow method histograms for R-134a data provided by Melo et al. [57] for diameter B (from Figure 4.10)

opposite direction. This exercise shows that small errors in measured quantities can provide larger errors for the simulations. It must also be noted that while the change in accuracy associated with the roughness is several percent, the effect on the mass flow rate is much smaller than that of the diameter of the capillary tube. Therefore it can be noted that small errors associated with diameter measurement will have a larger effect on simulation accuracy than roughness measurement.
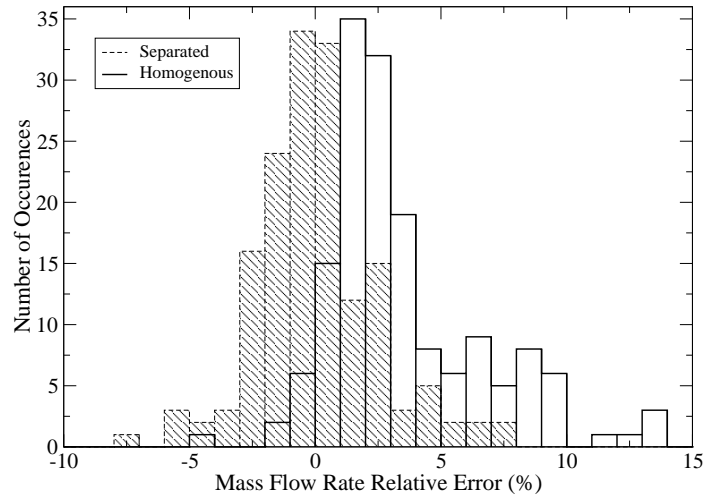
Figure 4.7: Homogenous and separated flow method histograms for R-134a data provided by Melo et al. [57] for diameter C (from Figure 4.10)
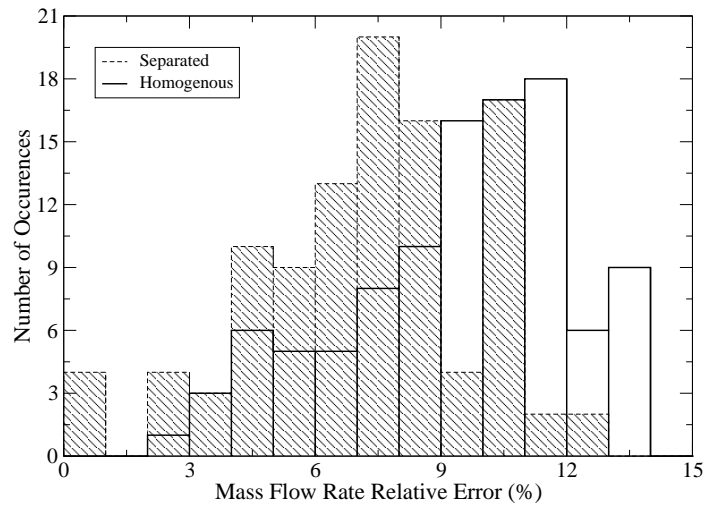
Figure 4.8: Homogenous and separated flow method histograms for R-134a data provided by Melo et al. [57] for diameter D (from Figure 4.10)

47
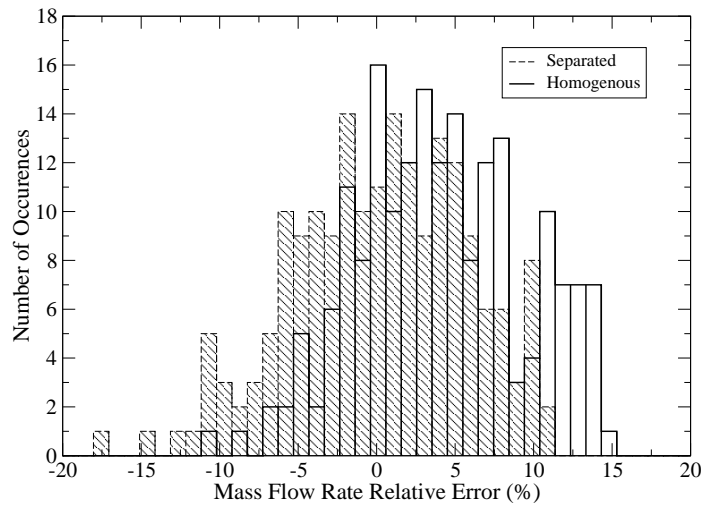
Figure 4.9: Homogenous and separated flow method histograms for Isobutane data provided by Melo et al. [57])
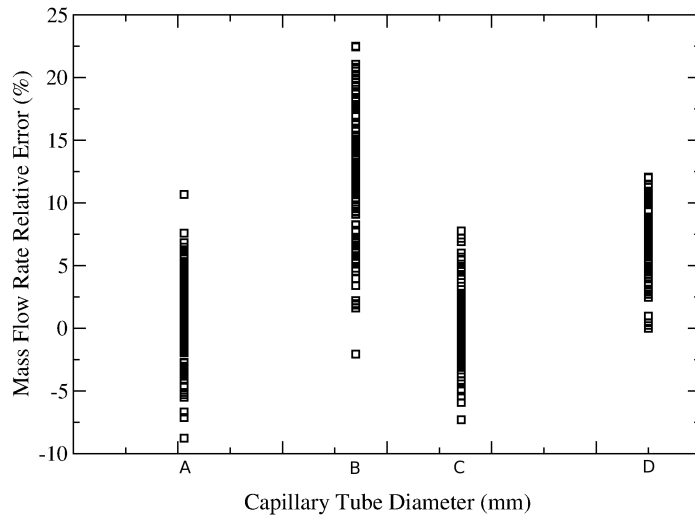
Figure 4.10: Mass flow rate relative errors, utilizing the separated flow method, compared to capillary tube diameters for experiments by Melo et al. [57] for R-134a
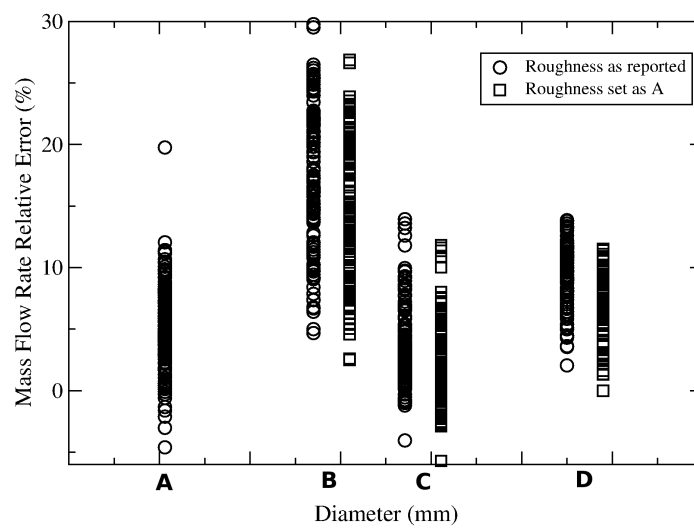
Figure 4.11: Mass flow rate relative errors, utilizing the homogenous flow method, for R-134a data provided by Melo et al. [57]) shown for diameters A, B, C, and D for roughness reported and for roughness set equivalent to diameter A

CHAPTER 5

EXPANDING METHODS TO ETHANOL AND CO$_2$ MIXTURES

In order to apply the presented methods to a mixture of carbon dioxide and ethanol, a procedure must be established within which the thermodynamic properties of the mixture can be established. The REFPROP program utilized earlier contains properties of pure carbon dioxide and ethanol, but does not contain the mixing rules that are vital to representing the thermodynamic data properly. Therefore a cubic equation of state will be manipulated to gain the necessary properties based upon the program GEFlash created by Neroorkar and Schmidt [65] for use with gasoline and ethanol blends.

5.1 Liquid and Vapor Densities Via The Cubic Equation of State

The cubic equation of state (CEOS) utilized for this model is the Peng-Robinson CEOS modified by Stryjek and Vera (PRSV) [68].

$$P = \frac{RT}{V - b} - \frac{a}{V^2 + ubV + wb^2} \tag{5.1}$$

Where u and w are constants dependant on the CEOS and are taken as $u = 2$ and $w = -1$ for PRSV. The variables a and b are defined using Equations (5.2) and (5.3), respectively.

$$a = \frac{0.457235R^2T_c^2}{P_c} \left[1 + f\omega \left(1 - T_r^{1/2}\right)\right]^2 \qquad (5.2)$$

$$b = \frac{0.077796RT_c}{P_c} \qquad (5.3)$$

Where R is the gas constant, T_c is the critical temperature, and P_c is the critical pressure. The value for $f\omega$ is given by the correlation shown in Equation (5.4).

$$f\omega = \kappa_0 + \kappa_1 \left(1 + T_r^{1/2}\right)(0.7 - T_r) \qquad (5.4)$$

Where T_r is the reduced temperature, κ_0 is found the acentric factor, ω, in Equation (5.5), and κ_1 is found via experimental results. The values of κ_1 are 0.04285 for carbon dioxide and -0.16816 for ethanol [33].

$$\kappa_0 = 0.378893 + 1.4897153\omega - 0.17131848\omega^2 + 0.019655\omega^3 \qquad (5.5)$$

In order to expand the CEOS to mixtures, the classical van der Waals mixing rules are applied, where a and b have contributions from each pure component and are given by Equations (5.6) and (5.7), respectively.

$$a = \sum_i \sum_j X_i X_j a_{ij} \qquad (5.6)$$

$$b = \sum_i X_i b_i \qquad (5.7)$$

The mixture component of a, a_{ij}, is given by Equation (5.8) and X_i is the mol fraction of component i. The pure component variables a_i and b_i use the already established

51

Equations (5.2) and (5.3). The constant k_{ij} is taken to be 0.06 as done for the CEOS developed by Secuianu et al. [73].

$$a_{ij} = (a_i a_j)^{1/2}(1 - k_{ij}) \tag{5.8}$$

Equation (5.7) has already taken into account the generally accepted method of setting the constant l_{ij} in Equation (5.9) to zero.

$$b_{ij} = \frac{b_i + b_j}{2}(1 - l_{ij}) \tag{5.9}$$

In order to solve for the vapor and liquid densities, the CEOS is manipulated into the form of a cubic compressibility, Z, equation, given by Equation (5.10) [68].

$$Z^3 - (1 + B^* - uB^*)Z^2 + (A^* + wB^{*2} - uB^* - uB^{*2})Z$$
$$-A^*B^* - wB^{*2} - wB^{*3} = 0 \tag{5.10}$$

The terms A^* and B^* are used to put the compressibility equation into a more easily programmable form and are given by Equations (5.11) and (5.12).

$$A^* = \frac{aP}{R^2 T^2} \tag{5.11}$$

$$B^* = \frac{bP}{RT} \tag{5.12}$$

Given a pressure and a temperature value, the cubic compressibility equation can be analytically solved for the three roots. The maximum root is then used to solve for the vapor density, via the compressibility, and the minimum root is used to solve for the liquid density [68]. The middle root is non-physical and is ignored.
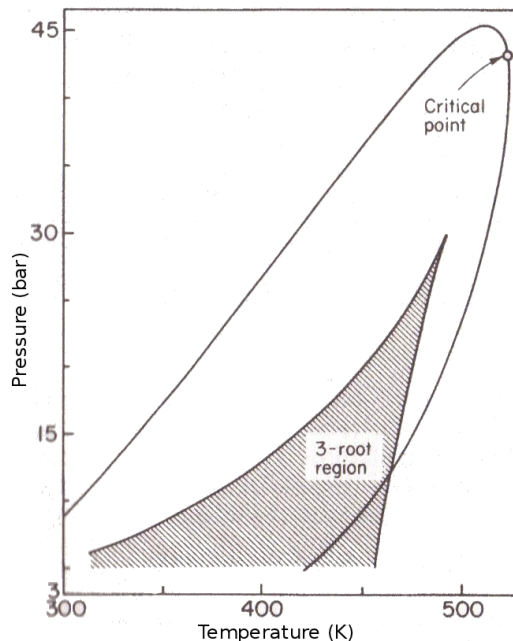
Figure 5.1: Phase behavior calculated by the Soave EOS for 26.54% ethane with 73.46% n-heptane [68]

5.1.1 Limitations Via the Trivial Root Problem

While solving the cubic compressibility equation is typically a process requiring little effort, there exists a caveat that makes the solution quite difficult to obtain for certain mixtures. For high pressure and/or temperature conditions, the cubic compressibility equation will only have one real root with two complex conjugate roots [18, 34, 53, 67]. When this occurs it is not known *a priori* if the one real root should be associated with the vapor or the liquid density. In the case of the mixture of 26.54% ethane and 73.46% n-heptane, shown in Figure 5.1, the three root region is shaded to show how small of a region is capable of utilizing the method. The trivial root problem can occur when the phases converge to identical compositions and are actually the same phase or when the volume of the phase with the current vapor composition is actually that of a liquid of the same composition and vice versa [68].

While Poling et al. [68] provides a sufficient overview of the problem, they do not guide the reader to any known solution technique. Furthermore personal communication with Dr. Mark McHugh, Professor of Chemical Engineering at Virginia Commonwealth University and expert in supercritical fluids, implied that there is no readily available or known solution to this problem [55, 56]

5.2 Viscosity Via Reichenberg Method

The viscosity of the mixture of carbon dioxide and ethanol can be found using the method of Reichenberg [68]. This method incorporates aspects of a kinetic theory approach with a corresponding states methodology. The mixture viscosity, η_m, is given by Equation (5.13) where the fluid is composed of n components.

$$\eta_m = \sum_{i=1}^{n} K_i \left(1 + 2 \sum_{j=1}^{i-1} H_{ij} K_j \sum_{\substack{j=1 \\ j \neq i}}^{n} \sum_{\substack{k=1 \\ k \neq i}}^{n} H_{ij} K_j K_k \right) \tag{5.13}$$

For a binary mixture it can be reduced to Equation (5.14).

$$\eta_m = K_1 \left(1 + H_{12}^2 K_2^2 \right) + K_2 \left(1 + 2 H_{12} K_1 + H_{12}^2 K_1^2 \right) \tag{5.14}$$

The components of K are found via Equations (5.15) and (5.16) using the pure component viscosity, η_i, and pure component molecular weight, M_i.

$$K_1 = \frac{X_1 \eta_1}{X_1 + \eta_1 \left(X_2 H_{12} \left[3 + \left(\frac{2M_2}{M_1} \right) \right] \right)} \tag{5.15}$$

$$K_2 = \frac{X_2 \eta_2}{X_2 + \eta_2 \left(X_1 H_{12} \left[3 + \left(\frac{2M_1}{M_2} \right) \right] \right)} \tag{5.16}$$

Components of H_{ij} are given by Equation (5.17).

$$H_{ij} = \left[\frac{M_i M_j}{32(M_i + M_j)^2}\right]^{1/2} (C_i + C_j)^2 \left[\frac{\left(1 + 0.36 T_{r_{ij}} \left[T_{r_{ij}} - 1\right]\right)^{1/6} F_{R_{ij}}}{(T_{r_{ij}})^{1/2}}\right] \quad (5.17)$$

The ij component of the reduced temperature, $T_{r_{ij}}$, is given by Equation (5.18),

$$T_{r_{ij}} = \frac{T}{(T_{ci} T_{cj})^{1/2}} \quad (5.18)$$

C_i is given by Equation (5.19),

$$C_i = \frac{M_i^{1/4}}{(\eta_i U_i)^{1/2}} \quad (5.19)$$

and $F_{R_{ij}}$ by Equation (5.20),

$$F_{R_{ij}} = \frac{T_{r_{ij}}^{3.5} + (10 \mu_{r_{ij}})^7}{T_{r_{ij}}^{3.5} \left[1 + (10 \mu_{r_{ij}})^7\right]} \quad (5.20)$$

where $\mu_{r_{ij}} = (\mu_{r_i} \mu_{r_j})^{1/2}$ and μ_{r_i} is the reduced dipole moment given by Equation (5.21).

$$\mu_{r_i} = 52.46 \frac{\mu_i^2 P_{c,i}}{T_{c,i}^2} \quad (5.21)$$

The dipole moment, μ, of ethanol is 1.69 and zero for carbon dioxide [68]. The U_i term is given by Equation (5.22).

$$U_i = \frac{[1 + 0.36 T_{r_i} (T_{r_i} - 1)]^{1/6} F_{R_i}}{(T_{r_{ij}})^{1/2}} \quad (5.22)$$

The i component of F_R is given by Equation (5.23).

$$F_{R_i} = \frac{T_{r_i}^{3.5} + (10 \mu_{r_i})^7}{T_{r_i}^{3.5} \left[1 + (10 \mu_{r_i})^7\right]} \quad (5.23)$$

5.3 Saturation Pressure

The method developed by Neroorkar and Schmidt [65], GEFlash, utilized the saturation pressure in the Clausius-Clapeyron equation, Equation (5.24).

$$\frac{dP_{sat}}{dT_{sat}} = \frac{H_{fg}}{T_{sat}\nu_{fg}} \tag{5.24}$$

Equation (5.24) can be rearranged to become Equation (5.25) if it is assumed that the specific volume of the liquid is negligible compared to the vapor and that the ideal gas equation is valid for the vapor phase.

$$\frac{(ln(P_{sat}))}{d(1/T_{sat})} = -\frac{H_{fg}}{R} \tag{5.25}$$

The intent of these assumptions is to put the Clausius-Clapeyron equation in a form that can be utilized to solve for the enthalpy of vaporization H_{fg} using the saturation properties and the gas constant R. For the gasoline and ethanol mixture GEFlash was written for the vapor pressure can be found using Equation (5.26), which was shown to effective by Pumphrey et al. [69].

$$P_{sat} = X_1\gamma_1 P_{1,sat} + X_2\gamma_2 P_{2,sat} \tag{5.26}$$

The activity coefficient, γ, is found via experimental data in Gmehling et al. [33]. This method was found to be acceptable for regions where the vapor pressure of the pure components $P_{i,sat}$ can be established via a lookup table. However, due to the already discussed differences between the critical properties of ethanol and carbon dioxide, coupled with the fact that saturation pressure is a function only of temperature, there exists a region above the critical point of carbon dioxide where Equation (5.26) cannot be used. When the desired temperature is above the critical temperature of carbon
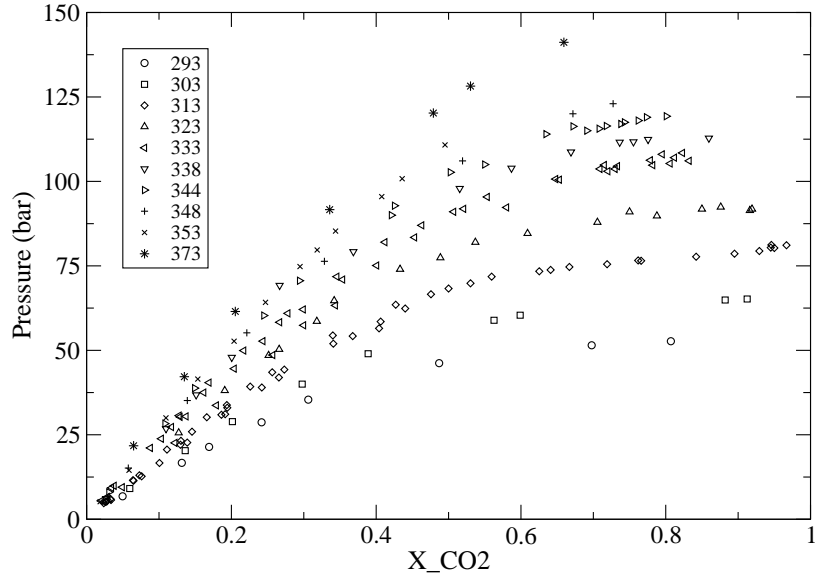
Figure 5.2: Vapor-Liquid Equilibrium (VLE) data collected from Secuianu et al. [73], Lim et al. [49], Suzuki et al. [76], Joung et al. [42], Garcia-Luna et al. [29], and Yeo et al. [88]

dioxide, there cannot be a pure component saturation pressure of the fluid, as the saturation pressure does not exist above the vapor dome.

In order to expand a vapor pressure estimation method beyond the critical temperature of carbon dioxide, experimental vapor-liquid equilibrium data were compiled from various literature at varying temperatures, shown in Figure 5.2 [73, 49, 76, 42, 29, 88]. Using the data, line fits can be created for each temperature that allows a user to provide a temperature and a carbon dioxide concentration, X_{CO2}, and return an interpolated value for the saturation pressure. So long as high concentrations of carbon dioxide, greater than 0.8, are avoided for temperatures greater than 323 K, the line fits should provide a sufficiently accurate interpolation.

5.4   Carbon Dioxide and Ethanol Mixture Results

Due to the trivial root problem encountered, this method for the mixture is severely limited in applicability, but is still capable of producing expansion results
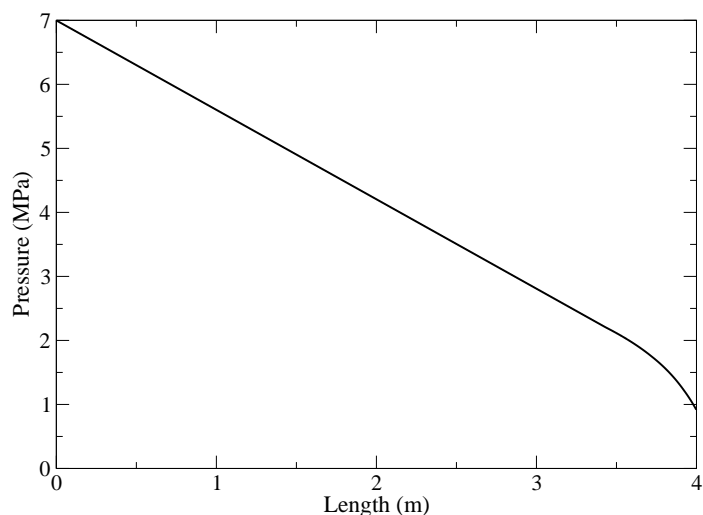
Figure 5.3: Pressure along the capillary tube for CO_2 and Ethanol Mixture where X_{CO2}=0.85

for low temperatures. Figures 5.3 and 5.4 show the expansion of pressure and velocity, respectively, across the capillary tube for a mixture with X_{CO2}=0.85 using the homogenous flow method. The homogenous flow method was utilized as it has been shown to be sufficiently accurate while requiring fewer thermophysical properties.

Validation for these cases is difficult to establish due to the limitations that the trivial root problem has imposed on the solution. Therefore the GEFlash program was modified to be capable of performing a simple VLE calculation based upon the method outlined in Poling et al. [68] and Ziervogel and Poling [91]. VLE calculations were performed for temperatures of 333 K and 338 K, shown in Figures 5.5 and 5.6 respectively, and are compared to experiments compiled by Secuianu et al. [73]. As illustrated in the figures, only calculations involving a high percent of ethanol avoid the trivial root due to the high temperature of these cases. When the results are compared to the experimental data they demonstrate that the equation of state can adequately predict the VLE data.

With the separated and homogenous flow methods each individually validated and the carbon dioxide and ethanol mixture model validated, the expansion of the

58
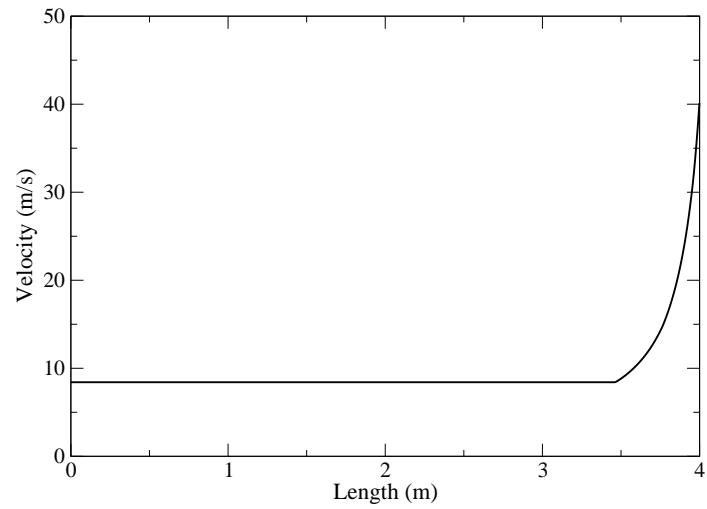
Figure 5.4: Velocity along the capillary tube for CO_2 and Ethanol Mixture where X_{CO2}=0.85

mixture can be considered validated. Until the trivial root problem can be solved and experimental results of a carbon dioxide and ethanol mixture expansion are produced the validation cannot attain such rigor as would normally be expected.
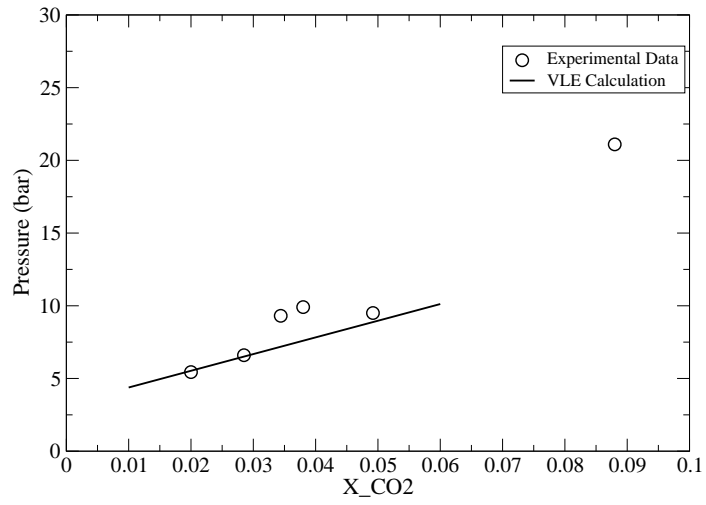
Figure 5.5: VLE diagram for T=333 K compared to experimental data compiled by Secuianu et al. [73]
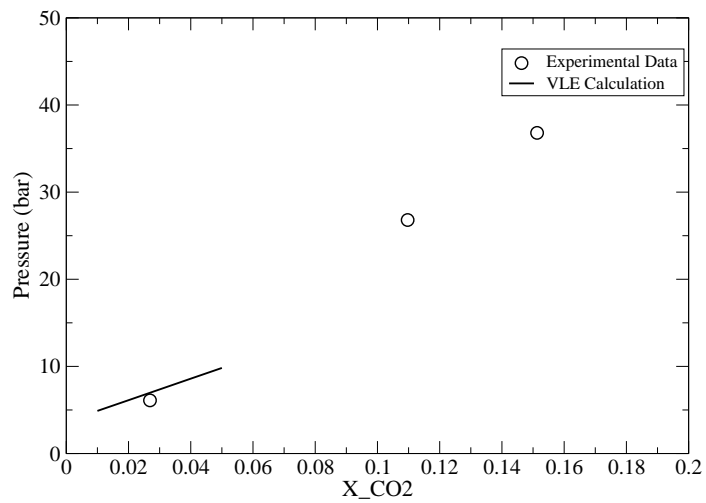
Figure 5.6: VLE diagram for T=338 K compared to experimental data compiled by Secuianu et al. [73]

CHAPTER 6

EXPANSION CHAMBER FLOW

Establishing an accurate method to model the flow through the capillary tube is just the first step in being able to model the entire PRESS process. Linking the one-dimensional capillary flow model to a two- or three-dimensional expansion chamber will be necessary before attempting to model any coagulation of particles due to the knowledge that significant growth can occur within the expansion chamber.

Preliminary work has already been done utilizing an open source computational fluid dynamics (CFD) software called OpenFOAM is utilized [85]. OpenFOAM contains a library of C++ codes that are utilized to create solvers for various applications. Many standard applications exist and can be used to as a basis for expanding the solver for use in more complex environments. The established rhoCentralFoam solver is used here, which is a density based compressible flow solver that utilizes the Kurganov and Tadmor central-upwinding schemes.

The expansion chamber can be modeled using a two-dimensional axisymmetric domain, shown in Figure 6.1. An axisymmetric boundary condition is utilized in order to reduce computation time, since it is known a priori that the solution is symmetric about the center of the capillary tube. The walls are configured such that they enforce the no slip boundary condition, while the expansion chamber outlet uses a wave transmissive outlet condition to set a far-field pressure to the ambient pressure of the expansion chamber. The inlet to the expansion chamber utilizes the pressure, temperature, and velocity conditions established at the outlet of the capillary tube. Figure 6.2 shows how the boundary conditions are enforced during the simulation.
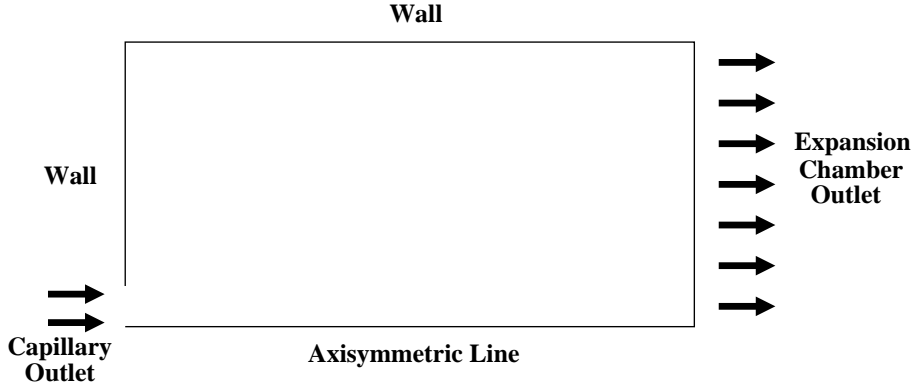
Figure 6.1: Boundary Conditions for Expansion Chamber Domain
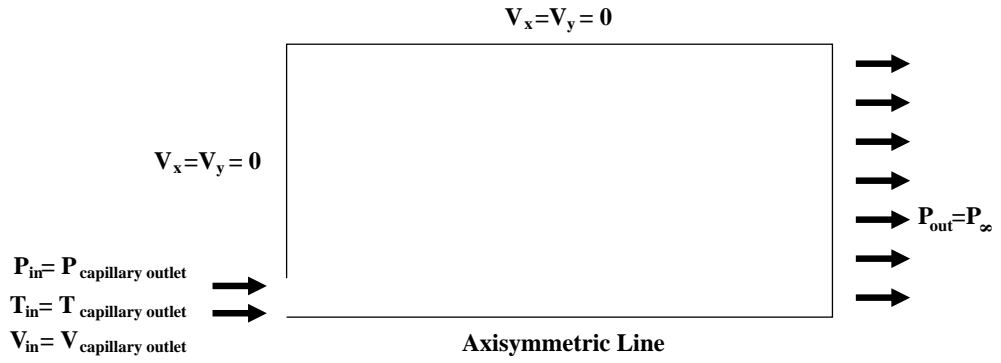
Figure 6.2: Explicit Variable Definitions for Expansion Chamber Domain Boundary

6.1 Preliminary Expansion Chamber Results

In order to verify the results of the OpenFOAM simulation the location of the Mach disk must be investigated. Figure 6.3 shows the Mach disk region of the expansion chamber and illustrates the velocity magnitude. By comparing the location of the Mach disk to the theoretical value, the results of the simulation can be verified. The theoretical value of the distance between the capillary exit and the Mach disk, found via wind tunnel experiments, is given by Equation (6.1) [5],

$$L_{Mach} = 0.67 d_i \sqrt{\frac{P_o}{P_{exp}}} \tag{6.1}$$

where P_o is the pressure at the outlet of the capillary tube and P_{exp} is the pressure of the expansion chamber. The geometry of Figure 6.3 has a capillary diameter of 127
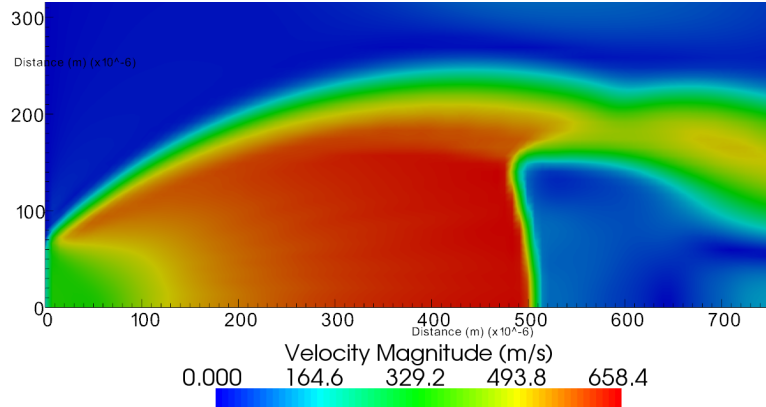
Figure 6.3: Velocity magnitude for the expansion chamber from the capillary exit to the Mach disk

μm with an outlet pressure of 2.61 MPa and atmospheric conditions in the expansion chamber. When inserted into the formula, the theoretical location of the Mach disk should be 432 μm from the capillary exit, which is comparable to the value seen in Figure 6.3 of approximately 500 μm. Furthermore, the diameter of the Mach disk can be compared to the theoretical value given by Equation (6.2) [5].

$$D_{Mach} = 0.5625 L_{Mach} \tag{6.2}$$

When the distance between the capillary exit and the Mach disk is inserted, the theoretical diameter of the Mach disk is found to be 243 μm. From Figure 6.3, the radius of the Mach disk can be estimated to be 143 μm, resulting in a diameter of 286 μm, which is comparable to the theoretical value.

The full expansion chamber from the simulation can be seen in Figure 6.4, which shows the expansion of CO_2 into the expansion chamber for the properties of pressure (Figure 6.4a), temperature (Figure 6.4b), and velocity (Figure 6.4c).
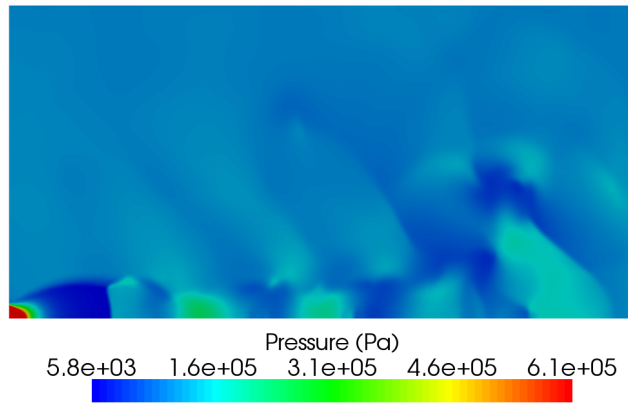
(a)
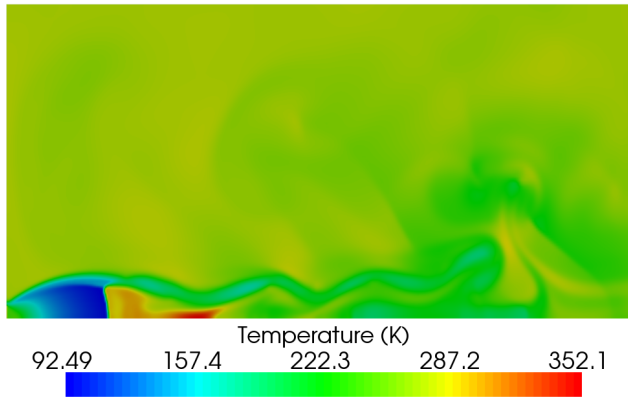
(b)
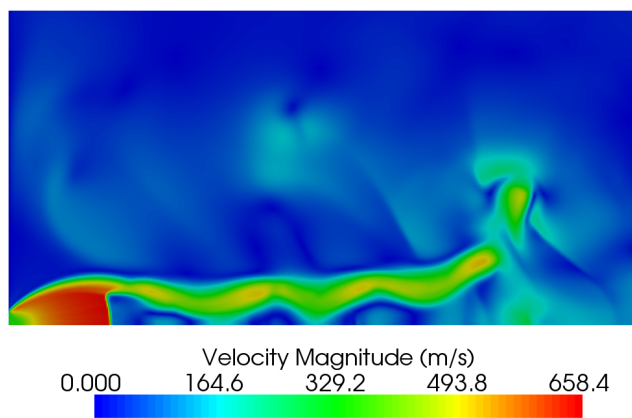
(c)

Figure 6.4: Expansion Chamber for the Expansion of Pure CO_2

64

CHAPTER 7

CONCLUSIONS

The homogenous and separated flow methods were implemented and validated such that a comparison of the accuracy could be established. Table 7.1 shows the mean errors for the three data sets for each method. It can be seen that the average error for both methods lie within the generally accepted margin of error. However, it is clear that the separated flow method consistently produces more accurate results than its homogenous counterpart. Furthermore, the separated flow method was shown to have a statiscally significant increase in accuracy over the homogenous flow method by looking at the histograms and performing the Kolmogorov-Smirnov and Wilcoxon Rank Sum Tests.

These results agree with the hypothesis that in the two phase region, the expansion process depends on the interactions between the vapor and liquid phases. These two phase interactions are important for deciding when to treat the flow as a vapor dispersed within the liquid or as an annular flow, where the liquid region is touching the walls and the vapor region is at the core of the capillary tube. They also take into account the large differences in density and viscosity between the two phases. By treating the two phases as one homogenous flow, the homogenous method loses important flow properties and therefore results in a slightly less accurate solution.

A method to expand the homogenous flow to a mixture of carbon dioxide and ethanol was implemented in a limited fashion. The trivial root problem limits the region where the compressibility equation can be analytically solved for its three real roots and therefore limits where an expansion process can be simulated. Within

	Homogenous Flow	Separated Flow
CO_2	8.13%	8.03%*
Isobutane	5.4%	4.57%
R-134a	8.55%	5.77%

Table 7.1: Mean mass flow rate relative errors for both the homogenous and separated flow methods for experiments conducted by da Silva et al. [19] and Melo et al. [57]. * Note that the result of the separated flow method does not include the point with an initial condition near the critical point.

the region of three real roots, the GEFlash program was utilized as a base code for producing thermophysical properties of carbon dioxide and ethanol mixtures. A viscosity model was added to the GEFlash program, using the method of Reichenberg, as prior editions did not require such a calculation. Furthermore, due to the drastic differences in critical properties, an estimation method for the saturation pressure when the mixture was above the critical temperature of carbon dioxide was required. The implementation within GEFlash required that a saturation pressure from both pure components exist and if the critical temperature of carbon dioxide is surpassed then this requirement can no longer be met. Therefore experimental vapor-liquid equilibrium data were utilized to create best fit lines for various temperatures greater than the critical temperature in order to create an estimation process requiring only the temperature and the mol fraction of carbon dioxide. The expansion of the carbon dioxide and ethanol mixture was successfully implemented at low temperatures and was validated through the use of a VLE diagram compared to experimental results.

CHAPTER 8

FUTURE WORK

8.1   Expansion Chamber Flow

As discussed in Chapter 6, the capillary tube flow needs to be coupled to the expansion chamber flow before a simulation involving the growth of particles along the capillary tube can be implemented. The simulation of supercritical fluids expanding through the capillary tube and into the expansion chamber play an important role in the design of PRESS process conditions. The PRESS process is designed to produce fine particles and the desired result of the particle sizes are as small as possible. As discussed in the literature review, particles continue to coagulate after the Mach disk. Therefore it is desirable for a simulation process to predict the inlet conditions to a capillary tube such that the flow is perfectly expanded to the pressure of the expansion chamber. Under these conditions, the expansion chamber will not have a Mach disk and it is hypothesized that smaller particles would result.

8.2   Solution to the Trivial Root Problem

The mixture of carbon dioxide and ethanol has gained significant interest over the last decade, therefore it will be important to be able to estimate the thermophysical properties over a wide range of conditions [78]. The cubic compressibility equation and its roots are useful for finding the thermophysical properties in a limited range, but without a larger area of accurate modeling techniques the area of interest for the mixture will be unable to be modeled.

8.3   Full Ternary PRESS Process

Once the expansion chamber has been coupled to the capillary tube for modeling purposes and the trivial root problem can be solved, then a full model of the PRESS process up to the plasma stream can be attempted. Using a carbon dioxide and ethanol mixture, along with a metallic precursor (possibly TiO_2) the expansion process within the capillary tube and expansion chamber can be coupled with aerosol equations to model the supersaturation and coagulation occurring during the expansion process. Once these steps have been implemented, the simulations can be utilized to help predict the best initial conditions for the desired results of the process.

APPENDIX

ADDITIONAL MATERIALS

A.1 Energy Equation Derivation

Starting from energy conservation:

$$\dot{m}\left(h + \frac{1}{2}V^2\right) = \dot{m}\left[(h + dh) + \frac{1}{2}(V + dV)^2\right] + dQ \qquad (A.1)$$

A.1.1 Adiabatic Flow

For adiabatic flow $dQ=0$:

$$\dot{m}\left(h + \frac{1}{2}V^2\right) = \dot{m}\left[(h + dh) + \frac{1}{2}(V + dV)^2\right] \qquad (A.2)$$

Rearranging the terms all onto the left side:

$$\dot{m}\left[\underbrace{h - h}_{0} + dh \underbrace{-\frac{1}{2}V^2 + \frac{1}{2}V^2}_{0} + \frac{1}{2}(dV)^2 + V\,dV\right] = 0 \qquad (A.3)$$

Using the definition of the velocity:

$$V = \frac{g}{\rho} \qquad (A.4)$$

$$\dot{m}\left[dh + \frac{1}{2}\left[d\left(\frac{g}{\rho}\right)\right]^2 + \frac{g}{\rho}d\left(\frac{g}{\rho}\right)\right] = 0 \qquad (A.5)$$

Noting that the mass flux must be constant and equal to the mass flow rate over the area:

$$g = const = \frac{\dot{m}}{A} \tag{A.6}$$

$$dh + \frac{g^2}{2}\left[d\left(\frac{1}{\rho}\right)\right]^2 + \frac{g^2}{\rho}d\left(\frac{1}{\rho}\right) = 0 \tag{A.7}$$

Inserting the following definition:

$$d\left(\frac{1}{\rho}\right) = -\frac{1}{\rho^2}d\rho \tag{A.8}$$

$$dh + \frac{g^2}{2}\left[-\frac{1}{\rho^2}d\rho\right]^2 - \frac{g^2}{\rho^3}d\rho = 0 \tag{A.9}$$

Assuming that $d\rho \neq 0$ due to its utilization as a constant step in discretizing the domain, the equation can be divided by $d\rho$ and rearranged:

$$\frac{dh}{d\rho} = \frac{g^2}{\rho^3} - \underbrace{\frac{g^2}{2\rho^4}d\rho}_{\approx 0} \tag{A.10}$$

The middle term on the right hand side is approximately zero, resulting in a final formulation.

$$\frac{dh}{d\rho} = \frac{g^2}{\rho^3} \tag{A.11}$$

A.2   Momentum Equation Derivation

Starting from conservation of momentum:

$$\rho\left(\underbrace{\frac{dV_z}{dt}}_{SS} + V_z\frac{dV_z}{dz}\right) = -\frac{dP}{dz} + \underbrace{\mu\left(\frac{d^2V_z}{dz^2}\right)}_{inviscid} - F \tag{A.12}$$

70

Assuming steady state and inviscid:

$$\rho V_z \frac{dV_z}{dz} = -\frac{dP}{dz} - F \tag{A.13}$$

Bringing the density inside of the derivative with the velocity to form a derivative of the mass flux:

$$V_z \underbrace{\frac{dg}{dz}}_{0} - V_z^2 \frac{d\rho}{dz} = -\frac{dP}{dz} - F \tag{A.14}$$

The mass flux must be constant and therefore its derivative is zero and dividing by ρ^2:

$$-\frac{V_z^2}{\rho^2}\frac{d\rho}{dz} = -\frac{1}{\rho^2}\frac{dP}{dz} - \frac{F}{\rho^2} \tag{A.15}$$

Inserting the Darcy friction factor:

$$F = \frac{fV_z^2\rho}{2d_i} \tag{A.16}$$

$$-\frac{V_z^2}{\rho^2}\frac{d\rho}{dz} = -\frac{1}{\rho^2}\frac{dP}{dz} - \frac{fg^2}{2\rho^3 d_i} \tag{A.17}$$

Inserting the definition of velocity:

$$V_z = \frac{g}{\rho} \tag{A.18}$$

$$-\frac{g^2}{\rho^4}\frac{d\rho}{dz} = -\frac{1}{\rho^2}\frac{dP}{dz} - \frac{fg^2}{2\rho^3 d_i} \tag{A.19}$$

Multiply by dz and divide by $d\rho$:

$$-\frac{g^2}{\rho^4} + \frac{1}{\rho^2}\frac{dP}{d\rho} + \frac{fg^2}{2\rho^3 d_i}\frac{dz}{d\rho} = 0 \tag{A.20}$$

71

Get the $\frac{dz}{d\rho}$ term by itself:

$$\frac{dz}{d\rho} = \left[\frac{g^2}{\rho^2} - \frac{dP}{d\rho}\right]\frac{2\rho d_i}{fg^2} \tag{A.21}$$

A.3 Adiabatic Capillary Experimental Data

Tables A.1 and A.2 show the experimental data taken from Silva et al. [19] while Tables A.3 and A.4 show a representative set of data from Melo et al. [57] using the capillary tube geometry listed in Table A.5.

A.4 Appendix D - Separated Flow Method for Adiabatic Process

This section describes the manipulation of Equations (4.2), (4.3), (4.4), and (4.7) into matrix form to be solved using Gauss elimination. Starting with Equation (4.2):

$$\frac{d}{dz}\left[(1-\alpha)\rho_l V_l + \alpha \rho_v V_v\right] = 0 \tag{A.22}$$

$$-\frac{d\alpha}{dz}\rho_l V_l + (1-\alpha)\frac{d\rho_l}{dz}V_l + (1-\alpha)\rho_l\frac{dV_l}{dz} + \frac{d\alpha}{dz}\rho_v V_v + \alpha\frac{d\rho_v}{dz}V_v + \alpha\rho_v\frac{dV_v}{dz} = 0 \tag{A.23}$$

Put the derivatives of the variables we are solving for one one side:

$$(1-\alpha)\rho_l\frac{dV_l}{dz} + \alpha\rho_v\frac{dV_v}{dz} - (\rho_l V_l - \rho_v V_v)\frac{d\alpha}{dz} = -(1-\alpha)V_l\frac{d\rho_l}{dz} - \alpha V_v\frac{d\rho_v}{dz} \tag{A.24}$$

Expanding Equation (4.3):

$$\frac{d}{dz}\left[(1-\alpha)\rho_l V_l^2\right] = -(1-\alpha)\frac{dP}{dz} - F_{Wl} + F_{lv} + V_i\frac{d}{dz}[(1-\alpha)\rho_l V_l] \tag{A.25}$$

$$-\rho_l V_l^2\frac{d\alpha}{dz} + (1-\alpha)V_l^2\frac{d\rho_l}{dz} + (1-\alpha)\rho_l\frac{dV_l}{dz}2V_l =$$

$$-(1-\alpha)\frac{dP}{dz} - F_{Wl} + F_{lv} + V_i\left[-\rho_l V_l\frac{d\alpha}{dz} + (1-\alpha)V_l\frac{d\rho_l}{dz} + (1-\alpha)\rho_l\frac{dV_l}{dz}\right] \tag{A.26}$$

Test Number	L	D	P_{in}	T_{in}	ρ_{in}	$\dot{m}_{exp}$	$\dot{m}_H$	$\dot{m}_S$
Units	m	mm	MPa	K	kg/m^3	kg/hr	kg/hr	hg/hr
1	4.0	0.55	11.50	305.85	777.71	6.79	6.773	6.546
2	4.0	0.55	11.50	318.65	626.08	5.94	5.814	5.588
3	4.0	0.55	8.00	301.45	731.86	5.15	5.027	4.620
4	4.0	0.55	8.00	307.65	483.82	4.46	4.007	4.098
5	2.0	0.55	11.50	305.75	778.60	9.08	9.518	9.303
6	2.0	0.55	11.50	318.45	629.22	7.91	8.171	8.000
7	2.0	0.55	8.00	301.25	734.99	6.66	7.046	6.637
8	2.0	0.55	8.00	307.45	511.68	5.53	5.723	5.233
9	2.0	0.83	11.50	305.75	778.60	24.03	27.342	27.405
10	2.0	0.83	11.50	318.55	627.66	22.46	23.283	23.672
11	2.0	0.83	8.00	301.25	734.99	19.24	19.841	19.660
12	2.0	0.83	8.00	305.55	499.38	16.28	15.174	16.020
13	4.0	0.64	11.50	305.85	777.71	9.32	10.015	9.793
14	4.0	0.64	11.50	318.45	629.22	8.17	8.605	8.403
15	4.0	0.64	8.00	301.35	733.44	6.90	7.391	6.935
16	4.0	0.64	8.00	307.65	483.82	5.51	5.854	5.298
17	4.0	0.83	11.50	305.75	778.60	19.48	19.584	19.475
18	4.0	0.83	11.50	318.45	624.50	17.14	16.586	16.879
19	4.0	0.83	8.00	301.25	734.99	14.22	14.290	13.911
20	4.0	0.83	8.00	307.75	469.68	11.82	11.068	10.727
21	2.0	0.64	11.50	305.75	778.60	13.50	14.045	13.855
22	2.0	0.64	11.50	318.45	629.22	11.75	12.029	11.910
23	2.0	0.64	8.00	301.45	731.86	9.65	10.294	9.878
24	2.0	0.64	8.00	307.55	497.98	7.97	8.241	7.813
25	4.0	0.55	11.00	315.25	652.65	5.92	5.809	5.556
26	4.0	0.55	8.50	307.85	622.85	4.89	4.743	4.331
27	2.0	0.55	11.00	314.85	658.84	7.85	8.187	7.958
28	2.0	0.55	8.50	306.95	650.28	6.43	6.790	6.413
29	2.0	0.83	11.00	315.05	655.76	22.62	23.256	23.502
30	2.0	0.83	8.50	306.75	655.61	18.85	19.156	19.136
31	4.0	0.64	11.00	314.95	657.30	8.14	8.605	8.374
32	4.0	0.64	8.50	306.95	650.28	6.65	7.132	6.693
33	4.0	0.83	11.00	314.95	657.30	17.08	16.732	16.715

Table A.1: Adiabatic Experimental Data from da Silva et al. [19]

Test Number	L	D	P_{in}	T_{in}	ρ_{in}	$\dot{m}_{exp}$	$\dot{m}_H$	$\dot{m}_S$
Units	m	mm	MPa	K	kg/m³	kg/hr	kg/hr	kg/hr
34	4.0	0.83	8.50	306.85	652.98	13.99	13.771	13.475
35	2.0	0.64	11.00	314.95	657.30	11.60	12.027	11.898
36	2.0	0.64	8.50	306.75	655.61	9.40	9.986	9.616
37	2.0	0.50	10.70	311.65	691.99	8.30	6.521	6.298
38	2.0	0.50	8.40	308.55	576.21	6.45	4.947	4.587
39	2.0	0.50	7.60	303.65	655.67	6.25	4.941	4.481
40	2.0	0.50	12.00	316.45	679.56	8.64	6.926	6.773
41	4.0	0.64	12.00	307.55	772.44	9.57	10.238	10.031
42	4.0	0.64	10.00	304.75	754.46	8.36	8.900	8.604
43	4.0	0.64	9.50	304.85	738.73	7.90	8.446	8.117
44	4.0	0.64	10.50	304.85	765.83	8.51	9.310	9.041
45	2.0	0.79	10.00	308.95	701.59	22.19	20.113	20.176
46	2.0	0.79	9.00	309.95	616.37	19.43	16.615	17.174
47	2.0	0.79	12.00	318.75	649.66	23.88	21.623	22.011
48	4.0	0.79	8.00	308.65	379.30	10.08	8.958	3.780
49	4.0	0.79	8.50	308.65	658.19	13.49	11.460	11.171
50	4.0	0.79	9.00	307.85	668.53	14.82	12.911	12.640
51	4.0	0.79	9.50	307.85	696.36	15.80	13.835	13.610
52	4.0	0.79	9.90	307.85	713.15	16.47	14.510	14.311
53	4.0	0.79	10.50	307.35	739.05	17.56	15.545	15.383
54	4.0	0.79	11.00	308.65	738.56	17.89	16.048	15.923
55	4.0	0.79	11.50	308.65	751.30	18.67	16.760	16.655
56	4.0	0.79	12.00	308.75	761.60	19.51	17.430	17.388
57	4.0	0.79	8.50	304.95	695.49	14.63	12.694	12.344
58	4.0	0.79	9.00	304.95	719.37	15.45	13.606	13.317
59	4.0	0.79	11.00	304.85	776.76	18.73	16.703	16.555
60	4.0	0.79	9.00	310.65	594.01	14.20	11.989	11.787
61	4.0	0.79	9.50	310.65	644.40	15.27	13.119	12.935
62	4.0	0.79	10.00	310.85	671.93	16.15	14.005	13.852
63	4.0	0.79	10.50	310.75	696.42	16.92	14.870	14.742
64	4.0	079	11.00	310.95	712.06	17.73	15.611	15.505
65	4.0	0.79	12.00	310.45	745.49	19.31	17.140	17.062
66	4.0	0.79	11.50	311.05	726.30	18.49	16.331	16.246

Table A.2: Adiabatic Experimental Data Continued from da Silva et al. [19]

Test Number	Tube	P_c	P_e	Sub-cooling	$\dot{m}_{exp}$	$\dot{m}_H$	$\dot{m}_S$
		bar	bar	K	kg/hr	kg/hr	kg/hr
1	1	7.21	0.97	4.2	2.0	2.34	1.96
2	1	7.23	1.03	7.6	2.4	2.66	2.2
3	1	7.27	1.04	12.0	2.5	2.83	2.48
4	1	7.13	1.0	13.8	2.3	2.92	2.55
5	1	9.23	0.96	3.7	2.11	2.7	2.25
6	1	9.17	0.97	8.6	2.37	3.01	2.6
7	1	9.29	0.98	12.8	2.8	3.23	2.89
8	1	11.25	0.98	10.7	2.89	3.38	3.06
9	1	11.19	0.98	15.7	3.15	3.65	3.36
10	4	7.29	0.96	5.1	2.71	2.91	2.49
11	4	7.29	0.96	7.2	2.81	3.14	2.66
12	4	7.26	0.97	10.5	2.94	3.24	2.91
13	4	9.24	1.04	3.5	2.9	3.19	2.72
14	4	9.25	1.04	6.9	2.89	3.42	3.04
15	4	9.23	1.05	10.0	2.99	3.58	3.29
16	4	9.2	0.99	14.5	3.67	3.83	3.62
17	4	11.26	0.96	3.3	3.14	3.54	3.07
18	4	11.2	0.98	7.6	3.31	3.83	3.46
19	4	11.18	1.05	14.5	3.78	4.27	4

Table A.3: Representative Adiabatic Experimental Data from Melo et al. [57] for Isobutane, where P_c is the pressure at the capillary tube inlet, P_e is the pressure at the outlet, and $\dot{m}_{exp}$, $\dot{m}_H$, and $\dot{m}_S$ are the mass flow rates from experiments, the homogenous flow assumption and the separated flow assumption, respectively. The capillary geometry is shown in Table A.5

Test Number	Tube	P_c	P_e	Sub-cooling	$\dot{m}_{exp}$	$\dot{m}_H$	$\dot{m}_S$
		bar	bar	K	kg/hr	kg/hr	kg/hr
1	1	9.26	0.98	3.4	3.32	4.22	3.49
2	1	11.28	0.96	5.6	3.63	4.91	4.28
3	1	14.3	1.02	6.3	4.26	5.55	5.03
4	3	11.23	0.98	3.9	8.72	10.03	9.1
5	3	11.22	1.07	8.3	9.67	10.99	10.37
6	3	14.23	1.21	5.6	10.34	11.9	11.08
7	4	9.14	0.99	4.8	4.0	5.17	4.47
8	4	14.26	1.03	11.22	6.3	7.26	6.87
9	6	11.21	1.27	4.0	11.18	14.0	11.19
10	6	11.25	1.37	8.2	12.14	13.22	12.73
11	6	14.26	1.56	6.2	13.08	14.46	13.81
12	6	14.23	1.73	13.3	15.01	16.52	16.11
13	7	9.1	1.08	9.5	2.21	2.49	2.16
14	7	11.06	1.02	5.7	2.17	2.62	2.17
15	7	14.13	1.0	7.5	2.7	3.05	2.64
16	8	9.03	1.08	6.4	5.04	5.99	5.29
17	8	11.09	1.06	7.4	5.92	6.74	6.15
18	8	14.03	1.11	4.4	6.87	7.28	6.5
19	8	15.05	1.19	7.2	7.45	7.93	7.3

Table A.4: Representative Adiabatic Experimental Data from Melo et al. [57] for R-134a, where P_c is the pressure at the capillary tube inlet, P_e is the pressure at the outlet, and $\dot{m}_{exp}$, $\dot{m}_H$, and $\dot{m}_S$ are the mass flow rates from experiments, the homogenous flow assumption and the separated flow assumption, respectively. The capillary geometry is shown in Table A.5

Tube	1	2	3	4	5	6	7	8
Internal diameter (mm)	0.77	0.84	1.05	0.77	0.84	1.05	0.606	0.871
Length (m)	2.926	3.027	3.020	2.009	1.993	2.030	2.998	2.973
Wall roughness (μm)	0.75	0.59	0.72	0.75	0.59	0.72	1.08	0.78

Table A.5: Tube Geometry for experiments conducted by Melo et al. [57] shown in Tables A.3 and A.4

Put the derivatives of the variables we are solving for one one side:

$$-\rho_l(V_i - 2V_l)(1 - \alpha)\frac{dV_l}{dz} + (1 - \alpha)\frac{dP}{dz} - \rho_l V_l(V_l - V_i)\frac{d\alpha}{dz} =$$
$$-F_{Wl} + F_{lv} + V_l(V_i - V_l)(1 - \alpha)\frac{d\rho_l}{dz} \qquad (\text{A.27})$$

Expanding Equation (4.4)

$$\frac{d}{dz}\left[\alpha\rho_v V_v^2\right] = -\alpha\frac{dP}{dz} - F_{Wv} - F_{lv} + V_i\frac{d}{dz}[\alpha\rho_v V_v] \qquad (\text{A.28})$$

$$\rho_v V_v^2\frac{d\alpha}{dz} + \alpha V_v^2\frac{d\rho_v}{dz} + 2\alpha\rho_v V_v\frac{dV_v}{dz} =$$
$$-\alpha\frac{dP}{dz} - F_{Wv} - F_{lv} + V_i\left[\rho_v V_v\frac{d\alpha}{dz} + \alpha V_v\frac{d\rho_v}{dz} + \alpha\rho_v\frac{dV_v}{dz}\right] \qquad (\text{A.29})$$

Put the derivatives of the variables we are solving for one one side:

$$\alpha\frac{dP}{dz} + \rho_v\alpha(2V_v - V_i)\frac{dV_v}{dz} - \rho_v V_v(V_i - V_v)\frac{d\alpha}{dz} =$$
$$-F_{Wv} - F_{lv} + \alpha V_v(V_i - V_v)\frac{d\rho_v}{dz} \qquad (\text{A.30})$$

Expanding Equation (4.7) with no heat transfer term:

$$\frac{d}{dz}\left[(1 - \alpha)\rho_l V_l\left(h_l + \frac{V_l^2}{2}\right) + \alpha\rho_v V_v\left(h_v + \frac{V_v^2}{2}\right)\right] = 0 \quad (\text{A.31})$$

$$-\rho_l V_l(h_l + \frac{V_l^2}{2})\frac{d\alpha}{dz} + (1 - \alpha)\rho_l(h_l + \frac{V_l^2}{2})\frac{dV_l}{dz} + (1 - \alpha)V_l(h_l + \frac{V_l^2}{2})\frac{d\rho_l}{dz} +$$
$$(1 - \alpha)\rho_l V_l\left(\frac{dh_l}{dz} + V_l\frac{dV_l}{dz}\right) + \rho_v V_v(h_v + \frac{V_v^2}{2})\frac{d\alpha}{dz} + \alpha\rho_v(h_v + \frac{V_v^2}{2})\frac{dV_v}{dz}$$
$$+\alpha V_v(h_v + \frac{V_v^2}{2})\frac{d\rho_v}{dz} + \alpha\rho_v V_v\left(\frac{dh_v}{dz} + V_v\frac{dV_v}{dz}\right) = 0 \quad (\text{A.32})$$

Put the derivatives of the variables we are solving for one one side:

77

$$\rho_l(1-\alpha)\left[\left(h_l+\frac{V_l^2}{2}\right)+V_l^2\right]\frac{dV_l}{dz}+\rho_v\alpha\left[\left(h_v+\frac{V_v^2}{2}\right)+V_v^2\right]\frac{dV_v}{dz}+$$

$$\left[\rho_vV_v\left(h_v+\frac{V_v^2}{2}\right)-\rho_lV_l\left(h_l+\frac{V_l^2}{2}\right)\right]\frac{d\alpha}{dz}=$$

$$-(1-\alpha)V_l\left[\left(h_l+\frac{V_l^2}{2}\right)\frac{d\rho_l}{dz}+\rho_l\frac{dh_l}{dz}\right]-\alpha V_v\left[\left(h_v+\frac{V_v^2}{2}\right)\frac{d\rho_v}{dz}+\rho_v\frac{dh_v}{dz}\right]\quad\text{(A.33)}$$

Putting Equations (A.24), (A.27), (A.30), and (A.33) into matrix form results in:

$$
\begin{bmatrix}
(1-\alpha)\rho_l & 0 & \alpha\rho_v & \rho_v V_v - \rho_l V_l \\[4pt]
\rho_l(2V_l - V_i)(1-\alpha) & 1-\alpha & 0 & \rho_l V_l(V_i - V_l) \\[4pt]
0 & \alpha & \rho_v\alpha(2V_v - V_i) & -\rho_v V_v(V_i - V_v) \\[4pt]
\rho_l(1-\alpha)\left[\left(h_l + \tfrac{V_l^2}{2}\right) + V_l^2\right] & 0 & \rho_v\alpha\left[\left(h_v + \tfrac{V_v^2}{2}\right) + V_v^2\right] & \rho_v V_v\left(h_v + \tfrac{V_v^2}{2}\right) - \rho_l V_l\left(h_l + \tfrac{V_l^2}{2}\right)
\end{bmatrix}
\frac{d}{dz}
\begin{bmatrix}
V_l \\ P \\ V_v \\ \alpha
\end{bmatrix}
$$

$$
+
\begin{bmatrix}
0 & -(1-\alpha)\dfrac{d\rho_l}{dz} & 0 & -\alpha\dfrac{d\rho_v}{dz} \\[8pt]
0 & (V_i - V_l)(1-\alpha)\dfrac{d\rho_l}{dz} & 0 & 0 \\[8pt]
0 & 0 & 0 & \alpha(V_i - V_v)\dfrac{d\rho_v}{dz} \\[8pt]
0 & -(1-\alpha)\left[\left(h_l + \tfrac{V_l^2}{2}\right)\dfrac{d\rho_l}{dz} + \rho_l\dfrac{dh_l}{dz}\right] & 0 & -\alpha\left[\left(h_v + \tfrac{V_v^2}{2}\right)\dfrac{d\rho_v}{dz} + \rho_v\dfrac{dh_v}{dz}\right]
\end{bmatrix}
\begin{bmatrix}
V_l \\ P \\ V_v \\ \alpha
\end{bmatrix}
=
\begin{bmatrix}
0 \\ -F_{Wl} + F_{lv} \\ -F_{Wv} - F_{lv} \\ 0
\end{bmatrix}
\tag{A.34}
$$

BIBLIOGRAPHY

[1] Abdulagatov, A.I., Stepanov, G.V., and Abdulagatov, I.M. The Critical Properties of Binary Mixtures Containing Carbon Dioxide: Experimental Data. *High Temperature 45* (2007), 85–126.

[2] Agrawal, Neeraj, and Bhattacharyya, Souvik. Adiabatic capillary tube flow in a transcritical carbon dioxide heat pump. In *7th IIR Gustav Lorentzen Conference on Natural Working Fluids* (Trondheim, Norway, May 2006).

[3] Agrawal, Neeraj, and Bhattacharyya, Souvik. Non-adiabatic capillary tube flow of carbon dioxide in a transcritical heat pump cycle. *Energy Conversion and Management 48* (2007), 2491–2501.

[4] Agrawal, Neeraj, and Bhattacharyya, Souvik. Homogeneous versus separated two phase flow models: Adiabatic capillary tube flow in a transcritical CO_2 heat pump. *International Journal of Thermal Sciences 47* (2008), 1555–1562.

[5] Ashkenas, H., and Sherman, F. S. The Structure and Utilization of Supersonic Free Jets in Low Density Wind Tunnels. In *Rarefied Gas Dynamics, Volume 2* (1965), J. H. de Leeuw, Ed., pp. 84–+.

[6] Bansal, P.K., and Rupasinghe, A.S. An homogenous model for adiabatic capillary tubes. *Applied Thermal Engineering 18* (1998), 207–219.

[7] Bansal, P.K., and Wang, G. Numerical analysis of choked refrigerant flow in adiabatic capillary tubes. *Applied Thermal Engineering 24* (2004), 851–863.

[8] Bansal, P.K., and Yang, C. Reverse heat transfer and re-condensation phenomena in non-adiabatic capillary tubes. *Applied Thermal Engineering 25* (2005), 3187–3202.

[9] Bennett, A., Lamm, S., Orbey, H., and Sandler, S.I. Vapor-Liquid Equilibria of Hydrocarbons and Fuel Oxygenates. *Journal of Chemical Engineering Data 38* (1993), 263–269.

[10] Bolstad, M.M., and Jordan, R.C. Theory and Use of the Capillary Tube Expansion Device. *Refrigerating Engineering 56*, 12 (1948), 519–523.

[11] Catchpole, O.J., Grey, J.B., and Noermark, K.A. Solubility of Fish Oil Components in Supercritical CO_2 and CO_2+Ethanol Mixtures. *Journal of Chemical Engineering Data 43* (1998), 1091–1095.

[12] Catchpole, O.J., Grey, J.B., and Noermark, K.A. Fractionation of fish oils using supercritical CO_2 and CO_2+ethanol mixtures. *Journal of Supercritical Fluids 19* (2000), 25–37.

[13] Charoenchaitrakool, M., Dehghani, F., Foster, N.R., and Chan, H.K. Micronization by Rapid Expansion of Supercritical Solutions to Enhance the Dissolution Rates of Poorly Water-Soluble Pharmaceuticals. *Ind. Eng. Chem. Res. 39* (2000), 4794–4802.

[14] Chen, Y., and Gu, J. Non-adiabatic capillary tube flow of carbon dioxide in a novel refrigeration cycle. *Applied Thermal Engineering 25* (2005), 1670–1683.

[15] Chernyak, Y., Henon, F., Harris, R.B., Gould, R.D., Franklin, R.K., Edwards, J.R., DeSimone, J.M., and Carbonell, R.G. Formation of Perfluoropolyether Coatings by the Rapid Expansion of Supercritical Solutions (RESS) Process. Part 1: Experimental Results. *Ind. Eng. Chem. Res. 40* (2001), 6118–6126.

[16] Churchill, S.W. Frictional equation spans all fluid flow regimes. *Chemical Engineering 84* (1977), 91–92.

[17] Cicchitti, A.E., Lombardi, C., Silvestri, M., Soldaini, G., and Zavattarelli, R. Two-phase cooling experiments – pressure drop, heat transfer and burnout measurements. *Energia Nucleare 7* (1960), 407–425.

[18] Coward, I., Gale, SE, and Webb, DR. Process engineering calculations with equations of state. *Chemical Engineering Research and Design 56*, a (1978), 19–27.

[19] da Silva, D.L., Hermes, C.J.L., Melo, C., Gonçalves, J. M., and Weber, G.C. A study of transcritical carbon dioxide flow through adiabatic capillary tubes. *International Journal of Refrigeration 32* (2009), 978–987.

[20] Danh, L.T., Truong, P., Mammucari, R., and Foster, N. Extraction of vetiver essential oil by ethanol-modified supercritical carbon dioxide. *Chemical Engineering Journal* (2010), doi:10.1016/j.cej.2010.08.048.

[21] Dobbs, J.M., Wong, J.M., Lahiere, R.J., and Johnston, K.P. Modification of Supercritical Fluid Phase Behavior Using Polar Cosolvents. *Industrial and Engineering Chemical Research 26* (1987), 56–65.

[22] Domingo, C., Berends, E.M., and van Rosmalen, G.M. Precipitation of ultrafine benzoic acid by expansion of a supercritical carbon dioxide solution through a porous plate nozzle. *Journal of Crystal Growth 166* (1996), 989–995.

[23] Domingo, Concepción, Berends, Edwin, and van Rosmalen, Gerde Maria. Precipitation of ultrafine organic crystals from the rapid expansion of supercritical solutions over a capillary and a frit nozzle. *Journal of Supercritical Fluids 10* (1997), 39–55.

[24] Duckler, A.E., Wicks, M., and Cleveland, R.G. Frictional pressure drop in two-phase flow part A and B. *American Institute of Chemical Engineers Journal 10* (1964), 38–51.

[25] Erth, R.A. *Two-phase flow in refrigeration capillary tubes: analysis and prediction.* PhD thesis, Purdue University, 1970.

[26] Esances, F., Pérez-Segarra, and Oliva, A. Numerical simulation of capillary-tube expansion devices. *International Journal of Refrigeration 18*, 2 (1995), 113–122.

[27] Fauske, H.K. Contribution to the theory of the two-phase, one-component critical flow. *Internal Report, Argonne National Laboratory, USA* (1962).

[28] Franklin, R.K., Edwards, J.R., Chernyak, Y., Gould, R.D., Henon, F., and Carbonell, R.G. Formation of Perfluoropolyether Coatings by the Rapid Expansion of Supercritical Solutions (RESS) Process. Part 2: Numerical Modeling. *Ind. Eng. Chem. Res. 40* (2001), 6127–6139.

[29] Galicia-Luna, L.A., Ortega-Rodriguez, A., and Richon, D. New apparatus for the fast determination of high-pressure vapor-liquid equilibria of mixtures and of accurate critical pressures. *Journal of Chemical Engineering Data 45* (2000), 265–271.

[30] García-Valladares, O., Pérez-Segarra, C.D., and Oliva, A. Numerical simulation of capillary-tube expansion devices behavious with pure and mixed refrigerants considering metastable region. Part II: experimental validation and parametric studies. *Applied Thermal Engineering 22* (2002), 379–391.

[31] García-Valladeres, O., Pérez-Segarra, C.D., and Oliva, A. Numerical simulation of capillary tube expansion devices behaviour with pure and mixed regriferants considering metastable region. Part I: mathematical formulation and numerical model. *Applied Thermal Engineering 22* (2002), 173–182.

[32] Ghoreishi, S.M., and Komeili, S. Modeling of fluorinated tetraphenylporphyrin nanoparticles size design via rapid expansion of supercritical solution. *Journal of Supercritical Fluids 50* (2009), 183–192.

[33] Gmehling, J., and Onken, U. *Vapor-liquid equilibrium data collection, chemistry data series.* DECHEMA, 2006.

[34] Gundersen, T. Numerical aspects of the implementation of cubic equations of state in flash calculation routines. *Computers & Chemical Engineering 6*, 3 (1982), 245–255.

[35] Hamburger, M., Baumann, D., and Adler, S. Supercritical Carbon Dioxide Extraction of Selected Medicinal Plants–Effect of High Pressure and Added Ethanol on Yield of Extraced Substances. *Phytochemical Analysis 15* (2004), 46–54.

[36] Helfgen, B., Hils, P., Holzknecht, Ch., Türk, M., and Schaber, K. Simulation of particle formation during the rapid expansion of supercritical solutions. *Aerosol Science 32* (2001), 295–319.

[37] Helfgen, B., Türk, M., and Schaber, K. Hydrodynamic and aerosol modeling of the rapid expansion of supercritical solutions (RESS-process). *Journal of Supercritical Fluids 26* (2003), 225–242.

[38] Hermes, C.J.L., Melo, C., and Gonçalves, J.M. Modeling of non-adiabatic capillary tube flows: A simplified approach and comprehensive experimental validation. *International Journal of Refrigeration 31* (2008), 1358–1367.

[39] Hirunsit, P., Huang, Z., Srinophakun, T., Charoenchaitrakool, M., and Kawi, S. Particle formation ibuprofen-supercritical CO_2 system from rapid expansion of supercritical solutions (RESS): A mathematical model. *Powder Technology 154* (2005), 83–94.

[40] İçen, H., and Gürü, M. Effect of ethanol content on supercritical carbon dioxide extraction of caffeine from tea stalk and fiber wastes. *Journal of Supercritical Fluids* (2010), doi:10.1016/j.supflu.2010.07.009.

[41] Ishii, M., and Hibiki, T. *Thermo-fluid dynamics of two-phase flow.* Springer, 2006.

[42] Joung, S.N., Yoo, C.W., Shin, H.Y., Kim, S.Y., Yoo, K.-P., Lee, C.S., and Huh, W.S. Measurements and correlation of high-pressure VLE of binary CO_2-alcohol systems (methanol, ethanol, 2-methoxyethanol and 2-ethoxyethanol). *Fluid Phase Equilibria 185* (2001), 219–230.

[43] Ksibi, H., and Subra, P. Influence of Nozzle Design on the Nucleation Conditions in the RESS Process. *Chem. Biochem. Eng. 10*, 2 (1996), 69–73.

[44] Kumar, S.K., and Johnston, K.P. Modelling the solubility of solids in supercritical fluids with density as the independent variable. *Journal of Supercritical Fluids 1*, 1 (1988), 15–22.

[45] Kwauk, Xianmin, and Debenedetti, Pablo G. Mathematical modeling of aerosol formation by rapid expansion of supercritical solutions in a converging nozzle. *Journal of Aerosol Science 24*, 4 (1993), 445–469.

[46] Lemmon, E.W., Huber, M.L., and McLinden, M.O. *NIST Standard Reference Database 23: Reference Fluid Thermodynamic and Transport Properties-REFPROP, Version 9.0.* National Institute of Standards and Technology Standard Reference Data Program, Gaithesburg, 2010.

[47] Li, Rui-Yang, Lin, Sui, Chen, Zu-Yao, and Zhi-Hang, Chen. Metastable flow of R12 through capillary tubes. *International Journal of Refrigeration 13* (1990), 181–186.

[48] Liang, S.M., and Wong, T.N. Numerical modeling of two-phase refrigerant flow through adiabatic capillary tubes. *Applied Thermal Engineering 21* (2001), 1035–1048.

[49] Lim, J.S., Lee, Y.-W., Kim, J.-D., Lee, Y.Y., and Chun, P.-S. Mass-transfer and hydraulic characteristics in spray and packed extraction columns for supercritical carbon dioxide-ethanol-water system. *Journal of Supercritical Fluids 8* (1995), 127–137.

[50] Lin, S., Kwok, C.C.K., Li, R.-Y., Chen, Z, H., and Chen, Z.-Y. Local frictional pressure drop during vaporization of R-12 through capillary tubes. *International Journal of Multiphase Flow 17*, 1 (1991), 95–102.

[51] Lockhart, R.W., and Martinelli, R.C. Proposed Correlation of Data for Isothermal Two-phase, Two-component Flow in Pipes. *Chemical Engineering Progress 45*, 1 (1949), 39–49.

[52] Madsen, Kenneth B., Poulsen, Claus S., and Wiesenfarth, Maike. Study of capillary tubes in a transcritical CO_2 regriferation system. *International Journal of Refrigeration 28* (2005), 1212–1218.

[53] Mathias, PM, Boston, JF, and Watanasiri, S. Effective utilization of equations of state for thermodynamic properties in process simulation. *AIChE journal 30*, 2 (1984), 182–186.

[54] McAdams, W.H., Wood, W.K., and Bryan, R.L. Vaporization inside horizontal tubes. II. benzene-oil mixture. *Transactions of the ASME 64* (1942), 193.

[55] McHugh, M.A., and Krukonis, V.J. *Supercritical Fluid Extraction – Principles and Practice.* Boston:Butterworths, 1986.

[56] McHugh, Mark. Personal communication. Virginia Commonwealth University, June 2011.

[57] Melo, C., Ferreira, R.T.S., Neto, C. Boabaid, Gonçalves, J.M., and Mezavila, M.M. An experimental analysis of adiabatic capillary tubes. *Applied Thermal Engineering 19* (1999), 669–684.

[58] Melo, C., Ferreira, R.T.S., Neto, C.B., Gonçalves, J.M., Pereira, R.H., and Thiessen, M.R. Evaluation of HC-600a, R134a and CFC-12 mass flow rates through capillary tubes. In *New Applications of Natural Working Fluids in Refrigeration and Air Conditioning, IIR* (Hannover, Germany, May 1995), pp. 621–630.

[59] Melo, C., Vieira, L.A.T., and Pereira, R.H. Non-adiabatic capillary tube flow with isobutane. *Applied Thermal Engineering 22* (2002), 1661–1672.

[60] Melo, Cláudio. Personal communication. Federal University of Santa Catarina, June 2011.

[61] Mendoza de la Cruz, J.L., and Galicia-Luna, L.A. High-pressure vapor-liquid equilibria for the carbon dioxide + ethanol and carbon dioxide + propan-1-ol systems at temperatures from 322.36 k to 391.96 k. *ELDATA: International Electron Journal of Physics-Chemistry Data 5* (1999), 157–164.

[62] Mikol, P. Adiabatic single and two-phase flow in small bore tubes. *Transactions of the Institution of Mining and Metallurgy* (1963), 75–86.

[63] Murga, R., Ruiz, R., Beltrán, S., and Cabezas, J.L. Extraction of Natural Complex Phenols and Tannins from Grape Seeds by Using Supercritical Mixtures of Carbon Dioxide and Alcohol. *Journal of Agriculture and Food Chemistry 48* (2000), 3408–3412.

[64] Nagahama, K., Suzuki, J., and Suzuki, T. High pressure vapor-liquid equilibria for the supercritical CO_2 + ethanol + water system. *Proceedings of International Symposium on Supercritical Fluids 1* (1988), 143–150.

[65] Neroorkar, K., and Schmidt, D. Modeling of Vapor-Liquid Equilibrium of Gasoline-Ethanol Blended Fuels for Flash Boiling Simulations. *Fuel* (2010).

[66] Oates, Gordon C. *Aerothermodynamics of Gas Turbine and Rocket Propulsion.* American Institute of Aeronautics and Astronautics, Inc., 1997.

[67] Poling, B.E., Grens, E.A., and Prausnitz, J.M. Thermodynamic properties from a cubic equation of state: avoiding trivial roots and spurious derivatives. *Industrial & Engineering Chemistry Process Design and Development 20*, 1 (1981), 127–130.

[68] Poling, B.E., Prausnitz, J.M., John Paul, O.C., and (Firm), Knovel. *The properties of gases and liquids*, vol. 5. McGraw-Hill New York, 2001.

[69] Pumphrey, JA, Brand, JI, and Scheller, WA. Vapour pressure measurements and predictions for alcohol-gasoline blends. *Fuel 79*, 11 (2000), 1405–1411.

[70] Saldaña, M.D.A., Zetzl, C., Mohamed, R.S., and Brunner, G. Extraction of Methylxanthines from Guaraná Seeds, Maté Leaves, and Cocoa Beans Using Supercritical Carbon Dioxide and Ethanol. *Journal of Agriculture and Food Chemistry 50* (2002), 4820–4826.

[71] Sami, Samuel M., and Maltais, H. Numerical modeling of alternative refrigerants to HCFC-22 through capillary tubes. *International Journal of Energy Research 24* (2000), 1359–1371.

[72] Schaeffer, S.T., Zalkoq, L.H., and Teja, A.S. Solubility of monocrotaline in supercritical carbon dioxide and carbon-dioxide-ethanol mixtures. *Fluid Phase Equilibria 43* (1988), 45–56.

[73] Secuianu, C., Feroiu, V., and Geană, D. Phase behavior for carbon dioxide + ethanol system: Experimental measurements and modeling with a cubic equation of state. *Journal of Supercritical Fluids 47* (2008), 109–116.

[74] Seixlack, A.L., and Barbazelli, M.R. Numerical analysis of refrigerant flow along non-adiabatic capillary tubes using a two-fluid model. *Applied Thermal Engineering 29* (2009), 523–531.

[75] Shaub, G.R., Brennecke, J.F., and McCready, M.J. Radial Model for Particle Formation from the Rapid Expansion of Supercritical Solutions. *Journal of Supercritical Fluids 8* (1995), 318–328.

[76] Suzuki, K., Sue, H., Itou, M., Smith, R.L., Inomata, H., Arai, K., and Saito, S. Isothermal Vapor-Liquid Equilibrium Data for Binary Systems at High Pressures: Carbon Dioxide-Methanol, Carbon Dioxide-Ethanol, Carbon Dioxide-1-Propanol, Methane-Ethane, Methane-1-Propanol, Ethane-Ethanol, and Ethane-1-Propanol Systems. *Journal of Chemical Engineering Data 35* (1990), 63–66.

[77] Teberikler, L., Koseoglu, S., and Akgerman, A. Selective Extraction of Phosphatidylcholine from Lecithin by Supercritical Carbon Dioxide/Ethanol Mixture. *Journal of the American Oil Chemists' Society 78*, 2 (2001), 115–120.

[78] Topliss, R.J. *Techniques to facilitate the use of equations of state for complex fluid-phase equilibria.* PhD thesis, University of California, Berkeley, 1985.

[79] Türk, M., Hils, P., Helfgen, B., Schaber, K., Martin, H.-J., and Wahl, M.A. Micronizaton of pharmaceutical substances by the Rapid Expansion of Supercritical Solutions (RESS): a promising method to improve bioavailability of poorly soluble pharmaceutical agents. *J. Supercritical Fluids 22* (2002), 75–84.

[80] Türk, Michael. Formation of small organic particles by RESS: experimental and theoretical investigations. *J. of Supercritical Fluids 15* (1999), 79–89.

[81] Wallis, G.B. *One-dimensional two-phase flow*, vol. 409. McGraw-Hill New York, 1969.

[82] Weber, M., Russell, L.M., and Debenedetti, P.G. Aerosol Formation in Supercritical Fluids with Explicit Particle Microphysics Simulation. *Annual AIChE Meeting, Miami Beach, Fl* (November, 1998).

[83] Weber, Markus, Russel, Lynn M., and Debenedetti, Pablo G. Mathematical modeling of nucleation and growth of particles formed by the rapid expansion of a supercritical solution under subsonic conditions. *Journal of Supercritical Fluids 23* (2002), 65–80.

[84] Weber, Markus, and Thies, Mark C. A simplified and generalized model for the rapid expansion of supercritical solutions. *Journal of Supercritical Fluids 40* (2007), 402–419.

[85] Weller, H.J., Tabor, G., Jasak, H., and Fureby, C. A tensorial approach to computational continuum mechanics using object-oriented techniques. *Computers in Physics 12*, 6 (1998), 620–631.

[86] Wongwises, Somchai, and Pirompak, Worachet. Flow characteristics of pure refrigerants and refrigerant mixtures in adiabatic capillary tubes. *Applied Thermal Engineering 21* (2001), 845–861.

[87] Xu, B., and Bansal, P.K. Non-adiabatic capillary tube flow: a homogenous model and process description. *Applied Thermal Engineering 22* (2002), 1801–1819.

[88] Yeo, S.D., Park, S.J., Jim, J.W., and Kim, J.C. Critical Properties of Carbon Dioxide + Methanol, + Ethanol, + 1-Propanol, and + 1-Butanol. *Journal of Chemical Engineering Data 45* (2000), 932–935.

[89] Yilmaz, Tuncay, and Ünal, Saban. General Equation for the Design of Capillary Tubes. *Transactions of the ASME 118* (1996), 150–154.

[90] Ziegler, J.W., Dorsey, J.G., Chester, T.L., and Innis, D.P. Estimation of Liquid-Vapor Critical Loci for CO_2-Solvent Mixtures Using a Peak-Shape Method. *Analytical Chemistry 67* (1995), 456–461.

[91] Ziervogel, RG, and Poling, BE. A simple method for constructing phase envelopes for multicomponent mixtures. *Fluid Phase Equilibria 11*, 2 (1983), 127–135.

[92] Zucker, Robert D., and Biblarz, Oscar. *Fundamentals of Gas Dynamics*. John Wiley and Sons, Inc., 2002.